AD_____

Award Number: W81XWH-09-1-0410

TITLE: Harnessing the Power of Light to See and Treat Breast Cancer

PRINCIPAL INVESTIGATOR: Nimmi Ramanujam, Ph.D.

CONTRACTING ORGANIZATION: Duke University
                                                            Durham, NC 27708
Á

REPORT DATE: October 201G
Á

TYPE OF REPORT: Annual
Á

PREPARED FOR: U.S. Army Medical Research and Materiel Command
                             Fort Detrick, Maryland 21702-5012
Á

DISTRIBUTION STATEMENT: Approved for Public Release;
                                             Distribution Unlimited
Á

The views, opinions and/or findings contained in this report are those of the author(s) and should not be construed as an official Department of the Army position, policy or decision unless so designated by other documentation.

REPORT DOCUMENTATION PAGE

Form Approved
OMB No. 0704-0188

1. REPORT DATE	2. REPORT TYPE	3. DATES COVERED
October 201G	Annual	18 September 201F – 17 September 201G

4. TITLE AND SUBTITLE

Harnessing the Power of Light to See and Treat Breast Cancer

5a. CONTRACT NUMBER

5b. GRANT NUMBER
W81XWH-09-1-0410

5c. PROGRAM ELEMENT NUMBER

6. AUTHOR(S)

Nimmi Ramanujam, Ph.D.

E-Mail: nimmi@duke.edu

5d. PROJECT NUMBER

5e. TASK NUMBER

5f. WORK UNIT NUMBER

7. PERFORMING ORGANIZATION NAME(S) AND ADDRESS(ES)

Duke University
Durham, NC 27708

8. PERFORMING ORGANIZATION REPORT NUMBER

9. SPONSORING / MONITORING AGENCY NAME(S) AND ADDRESS(ES)
U.S. Army Medical Research and Materiel Command
Fort Detrick, Maryland 21702-5012

10. SPONSOR/MONITOR'S ACRONYM(S)

11. SPONSOR/MONITOR'S REPORT NUMBER(S)

12. DISTRIBUTION / AVAILABILITY STATEMENT
Approved for Public Release; Distribution Unlimited

13. SUPPLEMENTARY NOTES

14. ABSTRACT

Our objective is to exploit the wealth of physiological, metabolic, morphological and molecular sources of optical contrast to develop novel strategies that focus on two breast cancer applications: tumor margin assessment and prediction of response to neo-adjuvant therapy. The proposed aims of this grant are expected to result in three major contributions. The first has the most immediate impact. An optically based strategy that can quickly and non-destructively detect positive tumor margins will decrease the need for re-excision surgery and thereby decrease the local recurrence rate and rate of distant metastases in women electing BCS. Gaining insight into the physiological, metabolic, morphological and molecular sources of heterogeneity within and among tumors and how they are modulated by therapy, drug resistance and metastatic potential will directly benefit prognostication, prediction of outcome and planning of cancer therapies. With these tools, clinicians and clinical researchers can get a better understanding of this disease and how it might react to a drug. Basic science researchers could use it as an informed approach to study tumor biology and assay the effect of novel therapeutic agents in vivo.

15. SUBJECT TERMS
optical spectroscopy, imaging, fiber-optic, molecular, screening, breast cancer

16. SECURITY CLASSIFICATION OF:			17. LIMITATION OF ABSTRACT	18. NUMBER OF PAGES	19a. NAME OF RESPONSIBLE PERSON USAMRMC
a. REPORT	b. ABSTRACT	c. THIS PAGE			19b. TELEPHONE NUMBER *(include area code)*
U	U	U	UU	Î €	

Table of Contents

1. INTRODUCTION:

Our objective is to exploit the wealth of physiological, metabolic, morphological and molecular sources of optical contrast to develop novel strategies that focus on two breast cancer applications: tumor margin assessment and prediction of response to neo-adjuvant therapy. The proposed aims of this grant are expected to result in three major contributions. The first has the most immediate impact. An optically-based strategy that can quickly and non-destructively detect positive tumor margins will decrease the need for re-excision surgery and thereby decrease the local recurrence rate and rate of distant metastases in women electing BCS. Gaining insight into the physiological, metabolic, morphological and molecular sources of heterogeneity within and among tumors and how they are modulated by therapy, drug resistance and metastatic potential will directly benefit prognostication, prediction of outcome and planning of cancer therapies. With these tools, clinicians and clinical researchers can get a better understanding of this disease and how it might react to a drug. Basic science researchers could use it as an informed approach to study tumor biology and assay the effect of novel therapeutic agents *in vivo*.

a. Original Statement of Work for 5 Years

Aim 1: Optical imaging of margin morphology on breast lumpectomy specimens: To evaluate the role of wide-field imaging (coverage) and high-resolution interrogation (localization) of breast margin morphology to guide surgical resection intra-operatively and pathologic assessment of the tumor margin post-operatively (Timeframe: year 1-5).

  1a. Development of one optical spectral imaging system that integrates sensing capabilities for aims 1 and 2 and a high-resolution probe that can image absorption, scattering and fluorescence contrast (timeframe, year 1).
  1b. Conduct clinical studies on lumpectomy margins on 200 patients (time frame, years 2-4)
  1c. Data analysis and interpretation (timeframe, years 3-5)
      Test the sensitivity and specificity of wide-field imaging to detect positive tumor margins
      Test sensitivity and specificity of high-resolution probe to detect IDC and DCIS.

Aim 2: Optical quantitative biology of different sub-types of breast cancer: To investigate biomarkers of oxygenation, carotenoids (β-carotene) and ECM proteins (collagen) in human breast cancer stratified by tumor sub-type and receptor status and their association with neo-adjuvant chemotherapy response.

  2a. Development of rotating needle compatible spectroscopy probe (timeframe, year 1).
  2b. Conduct clinical studies to measure optical biomarkers *in vivo* in 150 patients undergoing surgery (timeframe, years 2-4).
  2c. Conduct clinical studies to measure optical biomarkers from 75 patients before neo-adjuvant therapy
  2d. Data analysis and interpretation (years 3-5):
      Determine association of biomarkers with tumor subtype
      Determine association of biomarkers with receptor status

Determine association of biomarkers with genomic signatures

Determine association of biomarkers with pathologic sub-total and complete response

Aim 3: Optical quantitative biology to assess therapy response in different sub-types of breast cancer: To investigate biomarkers of oxygenation and ECM proteins (collagen and $\alpha_v\beta_3$ expression) in rodent breast cancer stratified by tumor sub-type, receptor status and metastatic potential in response to targeted and chemotherapies.

3a. To determine if multi-parametric intra-vital optical microscopy, measuring hemoglobin saturation, total hemoglobin, redox ratio, collagen, and integrin expression can monitor tumor response to tamoxifen in parental and tamoxifen-resistant MCF-7 tumors in the mouse dorsal skin fold window chamber (timeframe, years 1-2).

- A total of 40 athymic nude mice will be required for this study (10 mice/group).

3b. Monitor optical parameters in the dorsal skin fold window chamber in response to doxorubicin chemotherapy in MCF-7 parental and doxorubicin-resistant tumors (timeframe, years 2-3).

- A total of 40 athymic nude mice will be required for this study.

3c. Monitor optical parameters in the dorsal skin fold window chamber in response to doxorubicin chemotherapy in tumors that express high (MDA-435) and low (MCF-7) levels of $\alpha_v\beta_3$ integrin (timeframe, years 3-4).

- A total of 40 athymic nude mice will be required for this study.

3d. Data and statistical analysis (timeframe, year 5).

2. BODY:

Aim 1: ***Aim 1: Optical imaging of margin morphology on breast lumpectomy specimens:*** In Aim 1, our objective is to develop a strategy for high resolution fluorescence imaging of tumor margins, and to combine that with wide-field diffuse spectral imaging in a complementary fashion. For the high resolution fluorescence imaging component of the project, last year we demonstrated that preliminary application of sparse decomposition to high resolution images of acriflavine stained tissue shows promise for isolating individual tissue types and ultimately could allow for the automated detection of residual disease of surgical margins (see Aim 2 for additional information on high resolution imaging and development of the sparse decomposition algorithm). Additionally, we showed that both radiographic breast density and neoadjuvant status impact the spectroscopic data of the surgical margins and needs to be taken into account when diagnosing surgical margin status. Here we focus on advancing optical imaging for breast margin assessment by analyzing excisional time, cautery and patent blue dye on underlying sources of contrast in patients undergoing breast conserving surgery. We also present the implementation of the 49-channel device which enables acquisition of wide-field images of the tumor margins in a shorter amount of time combined with high resolution fluorescence imaging which enables imaging of tissue microanatomy.

Introduction

We have previously demonstrated that wide-field optical imaging of tumor morphology detects positive margins (margins with IDC and DCIS) with accuracies that well exceed that of the breast surgeon. Here we prospectively validate the wide-field imaging system that we have developed and further refine our understanding of the micro-architectural differences between different types of tumor margin sub-types, in particular, DCIS, towards improving sensitivity and specificity. Our approach is to image the boundaries of the excised tumor mass, which is consistent with the existing paradigm for post-operative pathologic margin assessment, using the 49-channel device to acquire wide-field images of the tumor margins and high resolution imaging of suspicious sites. In last year's report we showed that both radiographic breast density and neoadjuvant status impact the spectroscopic data of the surgical margins and needs to be taken into account when diagnosing surgical margin status. Since then we have further investigated the various sources of error on the optical properties of normal tissue and how these changes impact optical contrast and the accuracy of our predictive models. These results are described in more detail below.

  a. **Advancing optical imaging for breast margin assessment:** an analysis of potential sources of error (excisional time, cautery, and patent blue dye) on underlying sources of optical contrast

Breast conserving surgery (BCS) is a recommended treatment for early-stage breast cancer and for breast cancers that have been reduced in size by neoadjuvant therapy. The goal of BCS is to excise the tumor along with a margin of normal tissue, while preserving as much of the normal breast tissue as possible. Unfortunately, as many as 18-72% of patients undergoing BCS require repeat surgeries due to a close or positive surgical margin diagnosed post-operatively and thus, require a re-excision surgery to achieve cancer free margins [1-9]. The large variation in re-excisions is thought to be due to differences in surgeon's training, in the definition of a close margin, and in the perceived risk of focally positive margins versus extensive involvement [10].

Surgery to remove the cancer and obtain clear margins is a collaborative effort between the surgeon and the pathologist (and in some institutions, the radiologist). In spite of this, there can be substantial variability in the prediction of positive margins in the intra-operative and post-operative settings. Surgeons do not have adequate intra-operative assessment tools to ensure that the cancer has been completely removed at the time of first surgery. Pathologists do not have adequate tools for sampling from areas on large tumor margins. The lack of these capabilities represents a significant unmet clinical need for margin assessment for both the surgeon and pathologist.

Optical imaging of tissue is an attractive solution to this problem because it is relatively fast and non-destructive. Optical techniques can also measure features related to the histological landscape without the need for labels. Before this technology can be used in an intra-operative setting or in a post-operative setting, systematic studies have to be performed to determine

which surgical and post-surgical factors affect the precision and accuracy with which this technology maps optical contrast. This is true not only for our technology but other technologies, both optical and non-optical that are intended for this application. Specifically, if the technology is to be used on the excised margin (which is the way in which intra-operative pathology is performed), then there must be an understanding of how the presence of the blue sentinel lymph node mapping dye (referred to as patent blue dye) and cautery could influence the primary sources of contrast in the breast. Another important variable to characterize is the impact of the time delay after excision on the primary sources of optical contrast in the breast.

In this study, we examine the effects of time after excision on the following quantitative optical parameters in breast tumor margins which include: [β-carotene], oxygenated and deoxygenated hemoglobin, total hemoglobin concentration ([THb]), the wavelength-averaged reduced scattering coefficient from 450-600nm ($<\mu_s'>$), [β-carotene]/$<\mu_s'>$, [THb]/$<\mu_s'>$, hemoglobin saturation (HbSat), and and patent blue dye. In addition, we evaluate the effects of varying and patent blue dye concentration and cautery on the optical absorbers and scatterers. Finally, we evaluated how all of these results impact optical contrast between negative and close/positive margins for the purposes of breast tumor margin assessment.

Methods:
Details of the analysis of the diffuse reflectance data from the partial mastectomy specimens can be found in prior publications [11-14] and were discussed in previous reports. Briefly, spectra were corrected for daily variations in optical throughput using a Spectralon reflectance standard, and were normalized by the CCD integration time. An inverse Monte Carlo model [11, 15, 16] was used to obtain values for THb concentration, β-carotene concentration and the wavelength-averaged reduced scattering coefficient from 450-600 nm ($<\mu_s'>$), for each measured site (or pixel) on the specimen surface. Upon completion of the measurements, the measured sites were inked for histological correlation. The specimens were then transferred to the surgical pathology laboratory for routine pathologic processing, and following routine diagnostic workup the inked sites were evaluated microscopically by the study pathologist. The benign sites were classified as fat, fibro-adipose, fibro-glandular, or mixed/other; mixed/other refers to any site with some combination of fat, collagen, glands, or vessels. The malignant sites were classified as invasive ductal carcinoma (IDC), ductal carcinoma *in situ* (DCIS), or mixed/other; for these, mixed/other refers to sites with some combination of IDC, DCIS, or lobular carcinoma. If tumor cells extended to the inked surface, the margin was considered positive. If they were within 2 mm of the inked surface, the margin was considered close.

The extracted tissue parameters were fit to a longitudinal mixed-effects model, which is an appropriate method for evaluating the trends over time in optical measurements across different tissue types. Longitudinal models were performed in R version 2.7.2 (www.r-project.org) using the lme4 package. The fixed-effect terms in the models were the time from surgical excision of the specimen and the histological subtype of the measured site. This model resulted in a fitted slope for every measured site. In all tests of main effects and interactions, statistical significance was considered to be $p < 0.05$.

From March 2011 to September 2011, lumpectomies were analyzed from 10 patients resulting in 80 sites. A total of 7 sites were excluded due to poor probe-tissue contact. The tissue was submitted for histopathology on the remaining 73 sites. However, histopathology could only be obtained for 61 of the sites. From May 2009 to October 2010, mastectomies from 19 patients were analyzed, resulting in 38 individually-measured tissue sites. The optical parameters were plotted versus time for every site and inspected for trends; 4 sites were removed due to poor probe-tissue contact and/or motion artifacts observed in the data, 2 additional sites (1 patient) were removed because the optical measurements were made 85 minutes after excision which was much longer than the other sites. Of the remaining 32 sites, 20 had microscopic histological confirmation. Samples with histology confirmation were given an overall diagnosis of benign or malignant, and were then given a further classification by specific histological subtype.

Results:

Optical parameters affected by excision in lumpectomies
The purpose of doing these studies was to identify the optical parameters that are least affected by kinetics, the presence of patent blue dye, and cautery for optical margin assessment of lumpectomy specimens. Figure 1.1A-D show representative optical images of [β-carotene], [THb], and the ratios of [β-carotene] to $<\mu_s'>$ and THb to $<\mu_s'>$ for a negative (no residual carcinoma within 2 mm of the surface) margin and a positive margin. Histologically confirmed sites are highlighted corresponding to adipose, fibroadipose, or ductal carcinoma *in situ* (DCIS). Empirical cumulative distribution functions are shown in Figure 1.1E representing the distribution of the data in the negative and positive representative images. Both the margin-level data and site-level data show that [β-carotene]/$<\mu_s'>$ and [THb]/$<\mu_s'>$ decrease with malignancy and these were important parameters in differentiating margins in our previously published 48-patient study [12].
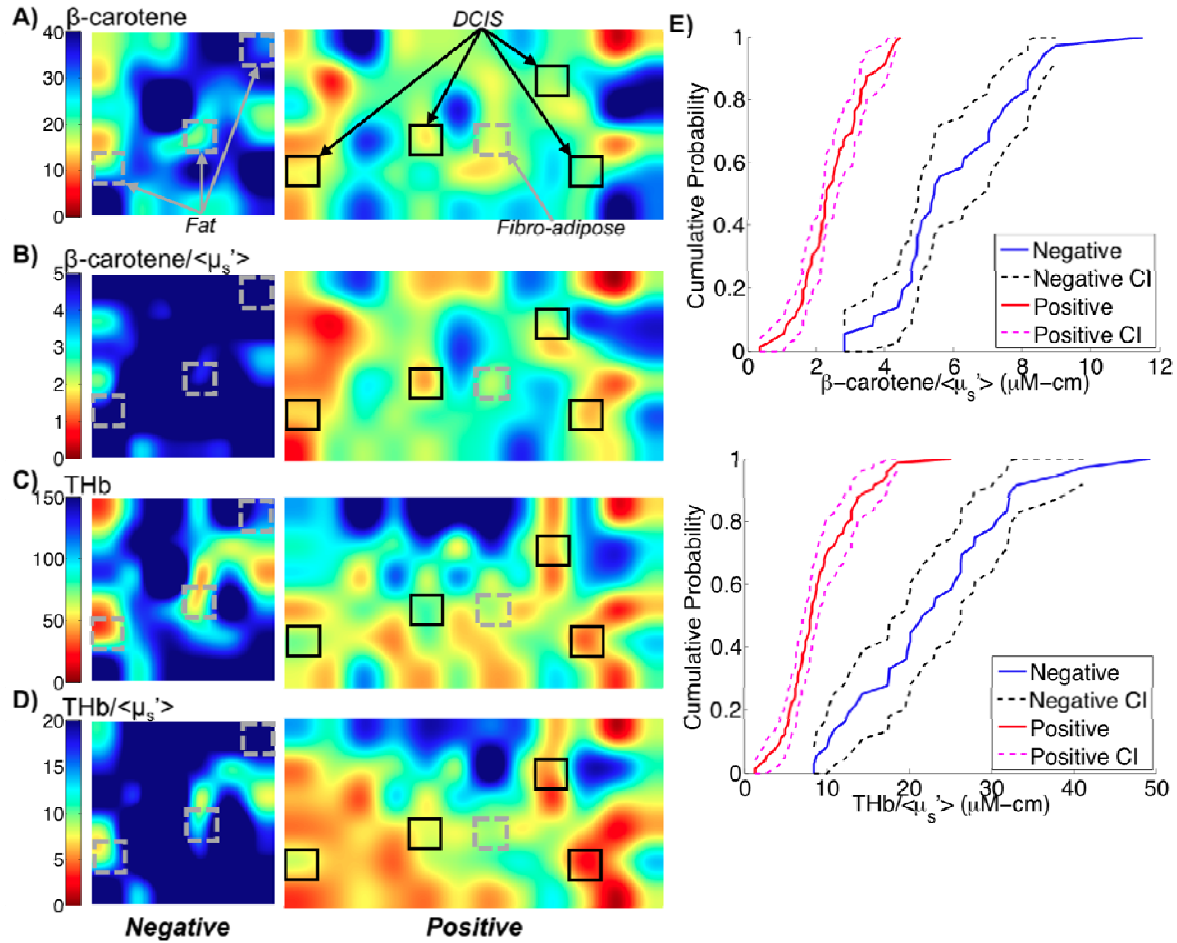
Figure 1.1: Example data acquired from lumpectomy margins in our previous study [12].
A-D) 50x bicubic interpolated images of β-carotene, β-carotene/$<\mu_s'>$, THb, and THb/$<\mu_s'>$ from a negative margin (3.5cm x 3.5cm) and a positive margin (3.5cm x 6.5cm). Benign (fat and fibro-adipose tissue) and malignant (ductal carcinoma in situ – DCIS) sites are highlighted. E) Cumulative distribution functions of the pixels in the negative and positive margins from the representative images along with their confidence intervals (CI).

Our first set of analyses examined the kinetics of lumpectomy specimens to determine how optical images of margins are impacted.   The linear longitudinal model was used to fit lumpectomy data from all 10 patients. Visually, β-carotene, $<\mu_s'>$, THb, and the ratios showed little change over time. HbSat as well as, oxy-hemoglobin and deoxy-hemoglobin exhibited marked changes over time and were not linear throughout the entire measurement window (data not shown). Therefore, oxy and deoxy-hemoglobin, and HbSat are not shown for the remainder of this manuscript for any analyses.

The rate of change could not be compared across tissue parameters because the units and magnitudes of the variables were not the same. Therefore, the percent change at various time points post-excision was calculated to identify the optical parameters with the smallest percent change. Figure 1.2 shows the percent change in the optical parameters. A maximum of 30 minutes is shown here to correspond with our previous lumpectomy study [12, 17-19] where the

average amount of time elapsed between excision and the end of imaging was 29 minutes. These results show that [β-carotene], $<\mu_s'>$, and [β-carotene]/$<\mu_s'>$ had the lowest percent changes over a 30 minute time window (median percent changes of -8.2, -13.8, and -8.0%). [THb] and [THb]/$<\mu_s'>$ had larger percent changes of -44.2% and -40.8% respectively; and [patent blue dye] had the largest percent change of -228.7%. This data was also evaluated for correlations between the first optical measurement and the time from excision. Spearman correlations were computed for all measured sites and no significant correlation was found between any of the optical parameters and time from excision to measurement, except for [patent blue dye] with p=0.0007. This was likely due to patent blue dye draining from the tissue after excision.
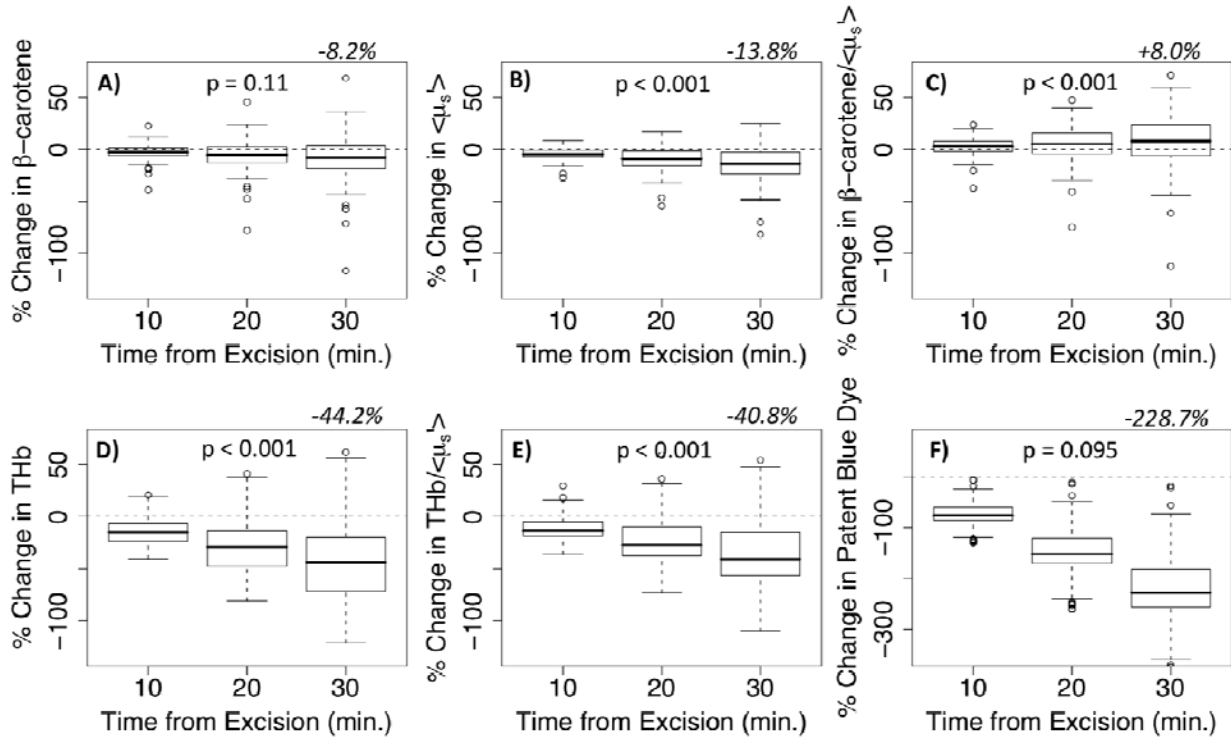

Figure 1.2: Percent change in each tissue parameter versus time from excision.
Predicted values of percent change; calculated as the fitted rate of change divided by the absolute value of the fitted intercept, multiplied by time from excision. Data is from histologically-confirmed lumpectomy sites (not all outliers are shown). The median percent change at 30 minutes is noted for each parameter along with a p-value denoting the significance of the fitted slope coefficient.

Effects of patent blue dye on optical absorption and scattering in the breast
In Figure 1.2 we showed that [patent blue dye] had the highest percent change over a 30 minute period and that it was correlated with time from excision. This led us to question whether the amount of patent blue dye would impact the other optical absorbers and scattering. Therefore, Monte Carlo simulations and a tissue mimicking phantom study were carried out to address this question. The simulated data covered the full range of absorption and scattering levels seen in our previous breast studies [18, 19], while the phantom data was for a subset of the breast optical properties that would result in the worst case scenario, i.e. where patent blue dye

dominates the absorption spectrum. The percent error in [THb], [β-carotene] (crocin for the phantoms), and $<\mu_s'>$ as a function of [patent blue dye] is shown in Figure 1.3 for both simulated and phantom data. The simulated data had negligible error, while the phantoms had slightly higher error attributed to experimental measurements. The simulated and phantom data both showed <3.3% error in extracted [THb], [β-carotene], and $<\mu_s'>$ even in the presence of high concentrations of patent blue dye (up to 80µM). With [THb] and [β-carotene] there did not appear to be any relationship of error with increasing [patent blue dye]. In the phantom data, when [patent blue dye] was approximately 10µM, $<\mu_s'>$ was underestimated by the model and as [patent blue dye] was increased, $<\mu_s'>$ was overestimated. This should not be a concern though as the percent error was <1.5% and the simulated results showed no trend. Overall, these results indicate that patent blue dye in concentrations up to 80µM do not impact the ability to quantify [THb] or [β-carotene], or $<\mu_s'>$ within the wavelength range of 450-600nm.

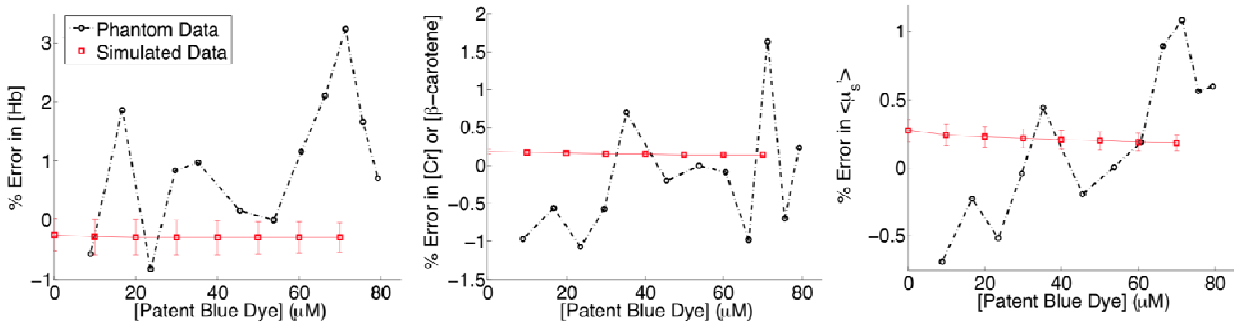**Figure 1.3: Average percent errors for Monte Carlo simulated data and phantom data.**
Data is shown for a single reference "phantom" ($<\mu_a>$=3.85cm^{-1}, $<\mu_s'>$=6.79cm^{-1} for the simulated data; $<\mu_a>$=3.02cm^{-1}, $<\mu_s'>$=5.81cm^{-1} for the phantom data). Simulated: 216 diffuse reflectance spectra were created consisting of 3 levels of scattering (4.85, 6.68, 9.15 cm^{-1}), THb (16.97, 31.03, 55.09 µM), and β-carotene (10.29, 16.29, 24.37 µM) and 8 levels of patent blue dye (0:10:70 µM). Phantom: patent blue dye was titrated 12 times (0-79µM) into a phantom consisting of 5.81cm^{-1} ($<\mu_s'>$), 16.69µM (THb), and 11.23µM (β-carotene).

Effects of cauterization on the optical parameters
Figure 1.4 shows the initial measurement of each optical endpoint separated by specimen type (lumpectomy or mastectomy). [THb] and [patent blue dye] were the only parameters that were significantly higher (p=0.013 and 0.0004, respectively) in the lumpectomies compared to mastectomies. We also examined the differences in the rates of change (constrained to a 10 minute time window) between mastectomy and lumpectomy benign sites (Figure 1.5). [β-carotene] and [β-carotene]/$<\mu_s'>$ were the only parameters that were not significantly (p=0.13 and 0.36 respectively) different between the two types of specimens.
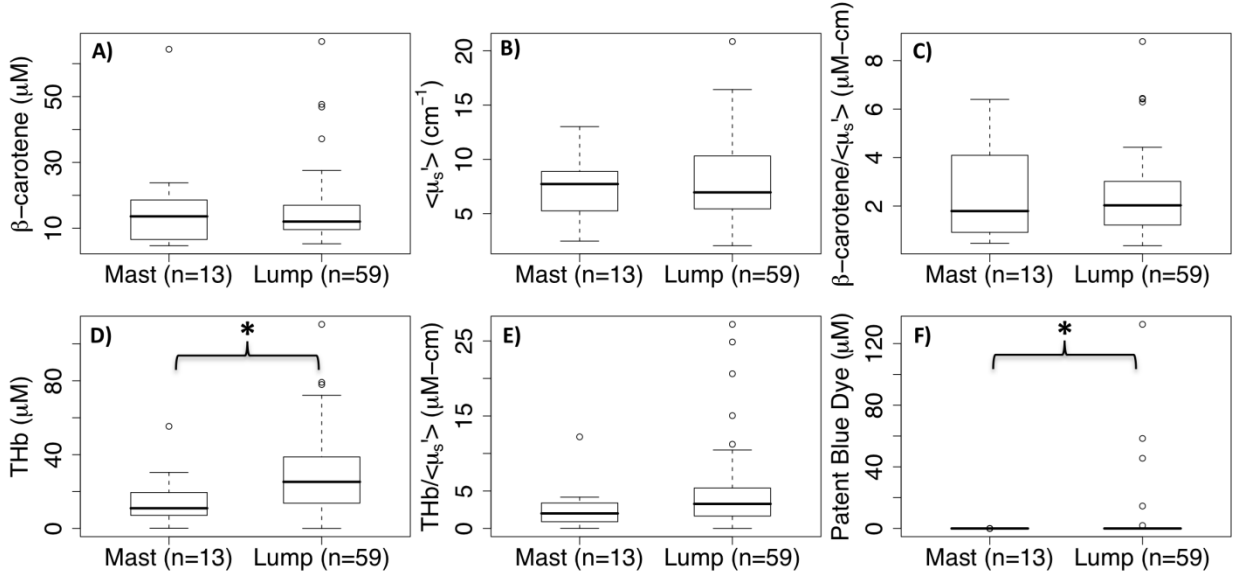
Figure 1.4: Optical parameters of the first measured time point.
Optical parameters of the first time point from the histologically-confirmed benign sites of mastectomies (Mast) and lumpectomies (Lump). * indicates p<0.05.
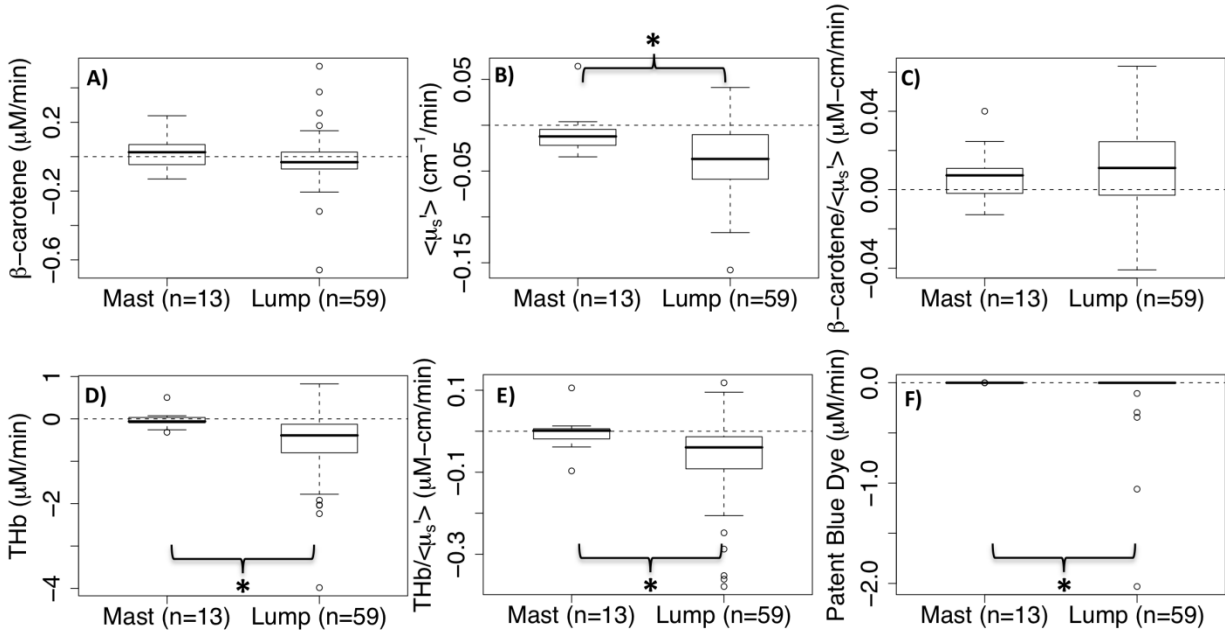

Figure 1.5: Rate of change in the tissue parameters.
Rate of change (fitted values from the model) in the tissue parameters from the histologically-confirmed benign sites of mastectomies (Mast) and lumpectomies (Lump) constrained to a time window of 10 min for all sites. * indicates p<0.05.

Kinetics in benign and malignant tissue

Figure 1.6 shows representative plots of two sites from two different patients, one measured with the shortest time from excision and the other with the longest time from excision. For each patient the histologically-confirmed benign and malignant site are shown. From the measured data we see that [β-carotene], $<\mu_s'>$, and [β-carotene]/$<\mu_s'>$ were relatively invariant with time as

was observed above. [THb] and [THb]/$\langle\mu_s'\rangle$ were also relatively invariant, although the benign site of Patient 1 had a slightly higher slope. The fitted data shown in this figure were from the longitudinal model. The model provided excellent fits to [THb], [β-carotene], $\langle\mu_s'\rangle$.
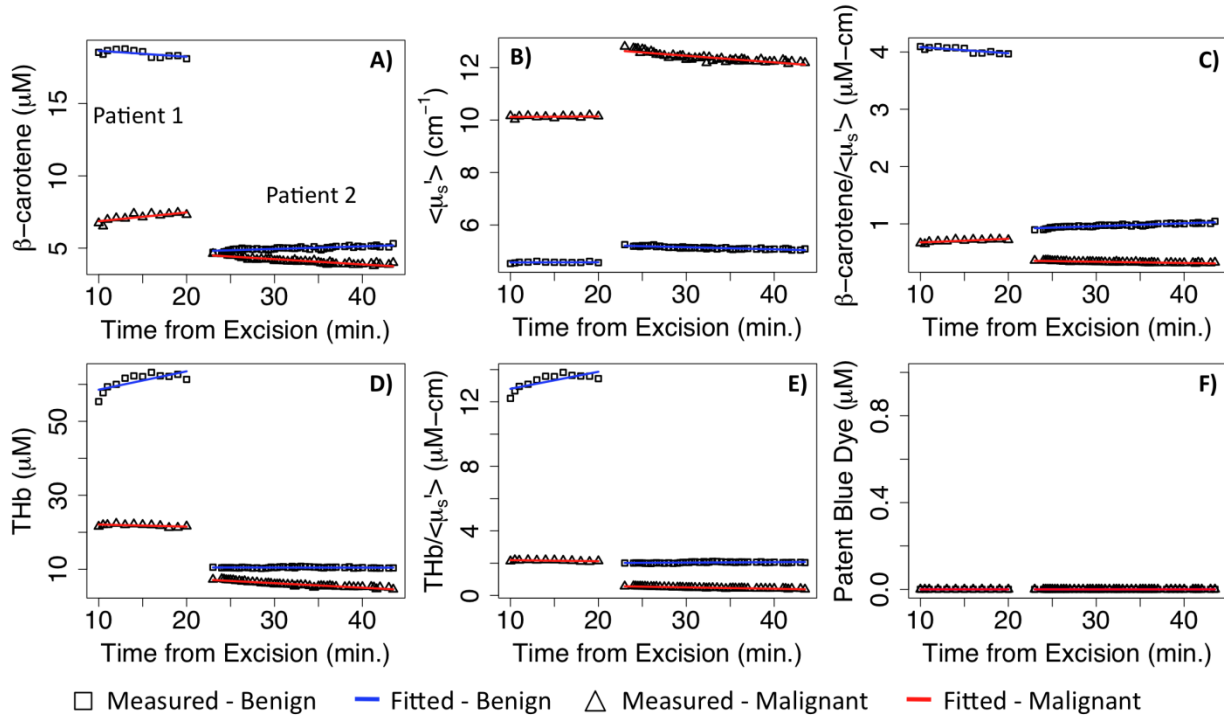

Figure 1.6: Example plots of kinetics in benign and malignant tissue.
Example plots of the tissue parameters versus time for four histologically known sites from two mastectomy patients. Symbols indicate the measured data lines are the model fits for the benign and malignant tissues.

Impact of kinetics on optical contrast for margin assessment
The results in this manuscript indicate that [β-carotene] and [β-carotene]/$\langle\mu_s'\rangle$ are the most robust variables but still change ~8% in 30 minutes. The question that arises is: what happens to contrast between negative and positive margins if a negative margin is imaged immediately after excision and a positive margin is imaged 30 minutes after excision, or vice versa? Figure 1.7 helps to illustrate the extent to which kinetics affect optical contrast. Images of a positive and negative margin from two different lumpectomies imaged at approximately the same time points post-excision are shown. The "initial" image is the actual parameter map that was measured. The median percent change for each variable at 10, 20, and 30 minutes post-excision (data from Section 3.2) was applied to either the negative or positive image to artificially decrease contrast. In Figure 1.7A this was implemented by multiplying the negative image by the median percent change. For [β-carotene], [THb], and [THb]/$\langle\mu_s'\rangle$, the percent change was in the negative direction and positive margins have lower values for these variables. To show the worst case scenario, the percent change was applied to the negative margin to decrease contrast. In Figure 1.7B, [β-carotene]/$\langle\mu_s'\rangle$ is lower in positive margins but increases over time; therefore, the percent change was applied to the positive margin to

decrease contrast. In Figure 1.7C, $<\mu_s'>$ is higher in positive margins but decreases over time, so the percent change was applied to the positive margin. These images show that an 8% change in [β-carotene] and [β-carotene]/$<\mu_s'>$ does not alter the contrast between the negative and positive margin. $<\mu_s'>$ contrast also does not change significantly; however the initial contrast is not as apparent. By 30 minutes, the >40% change in [THb] and [THb]/$<\mu_s'>$ greatly reduces the differences between the positive and negative margin; however, contrast is still preserved.
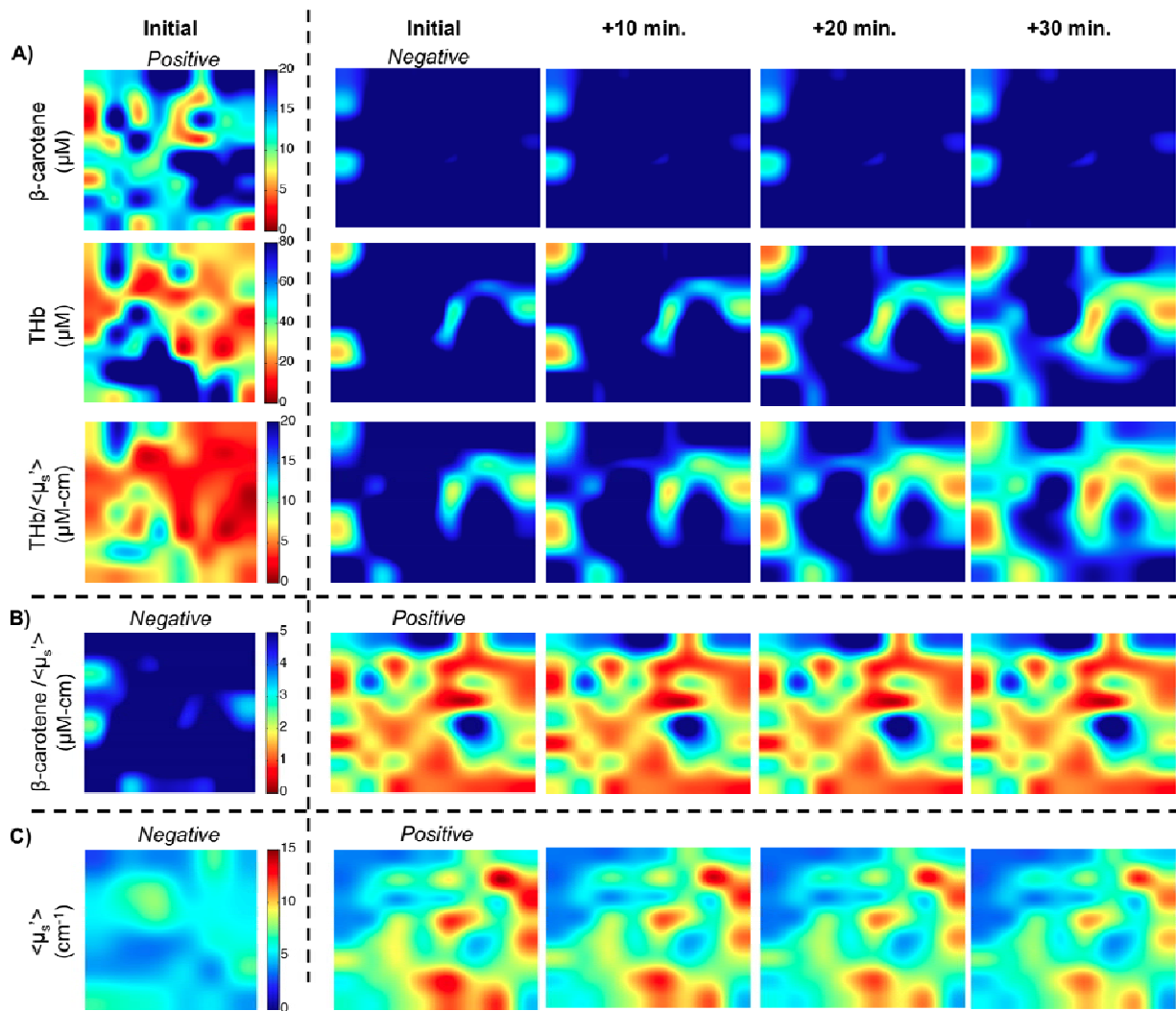
Figure 1.7: Effects of time on *ex vivo* spectral imaging.
50x bicubic interpolated images of a negative and positive margin from different patients, where the "initial" images of the margins were imaged at approximately the same time points post-excision. The "initial" images represent the actual data measured. The median percent change at 10, 20, and 30 minutes was applied to either the negative or positive image to show how an image would change if measured at various time points beyond the "initial" image time point. A) For β-carotene, THb, and THb/$<\mu_s'>$, the negative margins have higher values and the kinetics decrease over time. Therefore, the percent change is applied to the negative margin to show decreasing contrast (worst case scenario). B) For β-carotene/$<\mu_s'>$ the negative margins have higher values and the kinetics increase over time. C) For $<\mu_s'>$ the positive margins have higher values but the kinetics decrease over time.

Using our previous site-level data [18, 19], a percent difference was calculated between adipose and positive malignant sites; fibroadipose and positive sites; and fibroglandular and positive sites. These values were compared to the percent change at 10, 20, and 30 minutes for the lumpectomy kinetics data. The percent change is smaller than the percent difference for all optical parameters, indicating that optical contrast should be preserved within a 20 minute time window.

b. Using Breast Tissue Histology to Understand Optical Signatures and Improve Optical Margin Assessment:

Introduction:
Optical technologies are sensitive to underlying morphological composition and have the potential to provide surgeons with intra-operative margin assessment tools. The sources of optical scattering and demographic variations have not previously been deconstructed. Here, we evaluate ex-vivo breast tissue and corresponding quantified H&E images to correlate optical scattering signatures to the adipose, collagen and glandular content as well as variations with age, BMI and breast density.

Methods:
An ex-vivo study to evaluate partial mastectomy specimens with diffuse optical spectroscopy in patients undergoing surgery for breast malignancies was approved by the Institutional Review Board at Duke University as detailed in previous publications [12, 18]. The following patient characteristics were collected (if available): mammographic breast density (MBD), menopausal status, neo-adjuvant treatment status (chemotherapy or endocrine therapy), age, body mass index (BMI), and surgical re-excision status. Based on pre-operative mammograms, each patient was assigned an MBD based on a 4-point scale indicative of increasing amounts of fibroglanduar tissue: 1 (fatty), 2 (scattered fibroglandular), 3 (heterogeneously dense), or 4 (extremely dense). Women were designated as post-menopausal if they had one of the following: either a bilateral salpingo-oopherectomy or lack of a menstrual cycle for greater than 1 year.

Results:
Representative Data and Summary Variables
Representative margin parameter maps of [β-carotene] and $\langle\mu_s'\rangle$ with corresponding wavelength dependent μ_a, μ_s' spectra and histological images is shown in Figure 1.8. This figure demonstrates that adipose tissue contributes to increased β-carotene absorption and fibrogalndular tissue contribues to increased scattering, but it is unclear whether glands or collagen contribute more to scattering in the mixed tissues which contains glands, collagen and adipose tissue. This figure demonstrates that the collagen and glands are intrinsically linked together and both play a role in determining tissue scattering. Figure 1.8E&F were imaged with a 2.5x objective while Figure 1.8G was imaged with a 10x objective. The scale bars represent 500µm.
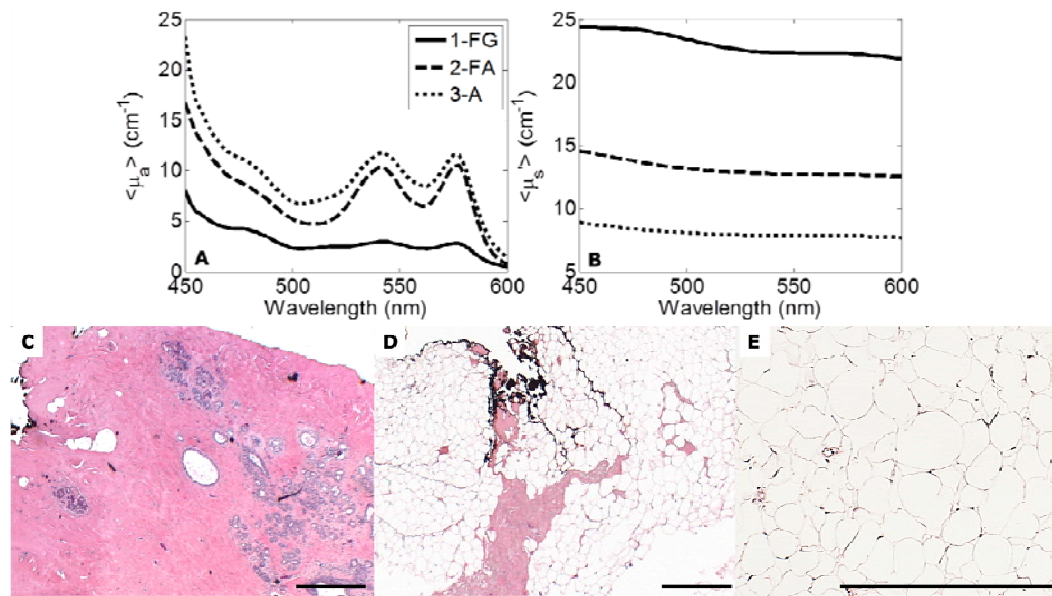
Figure 1.8: (A) The corresponding mean absorption coefficient (<μ$_a$>) and (B) the mean reduced scattering coefficient (<μ$_s$'>) for fibroglandular (FG), fibroadipose (FA) and adipose (A). The corresponding histology images for the fibroglandular (FG), fibroadipose (FA), and adipose (A) are shown in (C-E). This figure demonstrates adipose tissue contributes to increased β-carotene absorption and fibrogalndular tissue contribues to increased scattering. The scale bars represent 500 μm. The adipose H&E was imaged at 10x while the FG and FA images were acquired with a 2.5x objective.

Table 1.1 shows the mean and standard deviation for the optical and histological variables as a function of tissue type. The inter-rater agreement was κ=0.69 indicating a high degree of agreement across raters. Of the 394 total sites, 370 were benign and 24 were malignant. The benign tissue types were comprised of 213 adipose (A), 71 fibroadipose or collagen + adipose (FA), fibroglandular or collagen + glands (FG), and mixed tissue types comprised of collagen + adipose + glands (Mix). Due to the small sample size, the 24 malignant sites were grouped into one category (Mal). The highest scattering was seen in the FG sites followed by Mal, Mix and FA sites. [β-carotene] was the highest in Mal sites followed by A, FA, Mix and FG sites respectively. The percent adipose tissue increased in the following order: FG, Mal, Mix, and FA respectively. The percent collagen increased as follows: FA, Mix, Mal, and FG. The % glandular tissue was highest in Mal followed by FG and Mix; FA sites had minimal glandular tissue if any.

Table 1.1: Sample sizes, mean values and standard deviations for the optical and histological variables by tissue type. The mean and range of values demonstrate that FA has the highest % adipose, FG has the highest quantified collagen and μs', and Malignant have the highest quantified glandular parameters.

Tissue Type		n	<μ$_s$'>	[β-carotene]	% Adipose	% Collagen	% Glands
Benign		370	8.3 ± 4.0	20.2 ± 11.8	46.4 ± 29.4	47.3 ± 25.6	5.7 ± 7.2
	A	213	7.3 ± 3.1	21.5 ± 11	NA	NA	NA

FA	71	8.5 ± 3.9	20.9 ± 14.7	64.7 ± 23.0	34.5 ± 23.0	0.6 ± 1.1
FG	14	13.0 ± 7	13.6 ± 6.6	2.7 ± 3.0	81.4 ± 8.7	14.3 ± 8.8
Mix	72	10.3 ± 4.5	16.9 ± 10.5	36.9 ± 24.0	53.4 ± 21.8	9.1 ± 6.9
Malignant	**24**	**10.7 ± 4.3**	**28.1 ± 27.4**	**35.0 ± 30.5**	**41.7 ± 24.3**	**21.7 ± 19.6**

Patient Characteristics in sites with Low and High Percentages of Collagen

The 394 sites imaged were taken from 93 patients.

Table 1.2 shows the breakdown for the sites according to sites with either a low or high percentage of collagen using the median value (44%) of all sites as the cutoff. There was an even distribution of number of sites and patients with high and low percentage collagen. Sites were evenly distributed between MBD-2 and MBD-3. Sites from MBD-4 exhibited a higher fraction of collagen while sites from MBD-1 exhibited lower fractions of collagen, as expected. The sites with low percentage of collagen were from older patients ($p<0.00005$). Sites with a low percentage of collagen were also weighted towards post-menopausal patients consistent with increased age. Sites with higher fraction of collagen sites were evenly split between pre and post-menopausal patients; FG sites only fell into the higher percent collagen category but FA, Mix and Mal all exhibited high and low collagen morphologies. The cancer stage and invasive grade populated both high and low collagen categories.

Table 1.2: Summary table for the non-adipose H&E images and corresponding spectra. The data is separated to show the number of data points above and below the median % collagen. The summary shows the number of sites, MBD, age, menopausal status, tissue type, cancer stage and invasive grade. Sites with a high percentage of collagen were mostly from MBD of 2 or higher. FG sites had at least 56% or higher collagen.

		Collagen	
		<44%	**44-100%**
Patients		52	71
Sites		91	90
Breast Density			
	MBD1	18	5
	MBD2	32	29
	MBD3	38	34
	MBD4	3	21
	unknown MBD	0	1
Age		61±10.5	54.2±9.0
BMI		29.4±8.0	27.7±7.5
Menopausal Status			

Pre	12	42
Post	77	46
Unknown	2	2
Tissue Type		
FA	50	21
FG	0	14
Mix	27	45
Mal	14	10

Scattering vs. Collagen in Benign Sites

The relationship between $<\mu_s'>$ and percent collagen was examined; a positive correlation in benign sites is shown in Figure 1.9. $<\mu_s'>$ exhibited greater variability in sites with a higher percentage of collagen.
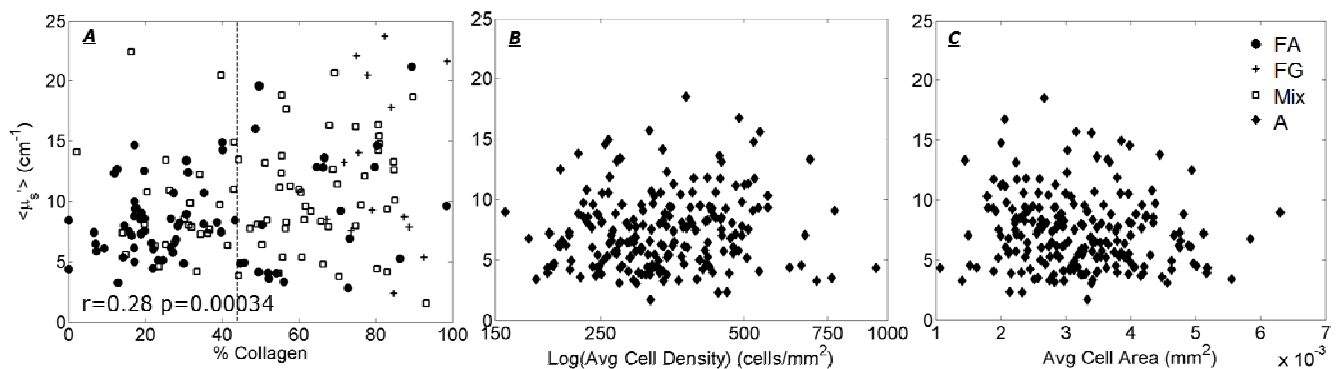

Figure 1.9: $<\mu_s'>$ is expected to be related to collagen and glands (nuclei and sub-nuclear components). When considering benign sites (FA, FG, Mix), $<\mu_s'>$ shows a positive correlation to the % collagen. The sites with collagen greater than 44% exhibit greater variability in $<\mu_s'>$ that cannot be explained by the % adipose tissue.

Effect of Patient Characteristics and percentage Collagen on Scattering

In order to investigate the relationship between the patient characteristics and morphology with respect to $<\mu_s'>$, the importance of each variable was analyzed after adjusting for percent collagen. The 213 adipose images were not included in this analysis. The correlations were examined by high and low percent collagen to determine whether the relationships changed with collagen level for benign sites (FA, FG, Mix) and all sites (FA, FG, Mix, Mal). The results of the correlations, linear fits and interactions are shown in Table 1.3. Age was negatively correlated to $<\mu_s'>$ in benign ($r=-0.32$, $p=4.7e-5$) and all ($r=-0.32$, $p=1.4e-5$) sites and this correlation varied significantly by the collagen level ($r=-0.40$ vs. -0.13). BMI was negatively correlated to $<\mu_s'>$ in benign ($r=-0.32$, $p=4e-5$) and all sites ($r=-0.31$, $p=2.8e-5$) but this relationship did not vary with collagen level.

Table 1.3: Each characteristic was fit as an independent variable with <µs'> as the dependent variable using Pearson's correlations and linear fits to establish relationships. Age and BMI were found to be independently associated with <µs'>. <µs'> decreased with both age and BMI but exhibited a stronger negative relationship to age in sites with a high percentage of collagen. MBD was positively correlated with <µs'> but not independent of Age and BMI.

	Benign		All Sites	
	r	p	r	p
Age	-0.32	4.7E-05	-0.32	1.4E-05
High % Collagen	-0.40	0.01	-0.37	0.02
Low % collagen	-0.13		-0.18	
BMI	-0.32	4.0E-05	-0.31	2.8E-05
High % Collagen	Ø	NS	Ø	NS
Low % collagen	Ø		Ø	
MBD	0.22	0.01	0.21	4.6E-03

Age, BMI, and MBD were found to be significant in describing $<\mu_s'>$. Age was found to vary with percentage collagen, resulting in a stronger correlation to $<\mu_s'>$ in sites with a high percentage of collagen. Age was correlated to BMI (r=0.36) but BMI remained significant in describing $<\mu_s'>$ after correcting for age. BMI did not have a dependence upon percentage collagen yet remained significant after adjusting for age by percent collagen.

Effects of Patient Characteristics and Adipocyte Morphology on Scattering
To determine whether or not adipocytes contributed to the correlation between collagen and $<\mu_s'>$, the relationship between $<\mu_s'>$ with adipocyte size and log (adipocyte density) as well as age and BMI is shown in Table 1.4 for the 213 adipose samples. Table 1.4 verified that this variability is not dependent upon the size and density of the adipocytes, nor age and BMI (p>0.05). Adipose tissues however, do contribute to a baseline scattering value. After adjusting the morphology components by breast density, a stronger relationship between ACA and $<\mu_s'>$ was seen in sites from high breast density patients (r=-0.29, p=0.026) but the relationship to cell density remained non-significant.

Table 1.4: <μ$_s$'> was not correlated to patient characteristics or adipocyte morphology in adipose sites; n=213, all p > 0.05. Average cell area (ACA) was significantly stronger in sites from high breast density patients (r=-0.29) vs low breast density patients (r=0.02).

		<μ$_s$'> (cm^{-1})	
		r	p
Age (years)		Ø	NS
	MBD1-2	Ø	NS
	MBD3-4	Ø	
BMI (kg/m^2)		Ø	NS
	MBD1-2	Ø	NS
	MBD3-4	Ø	
ACA (mm^2)		Ø	NS
	MBD1-2	**0.02**	**0.026**
	MBD3-4	**-0.29**	
Log(ACD) (cells/mm^2)		Ø	NS
	MBD1-2	Ø	NS
	MBD3-4	Ø	

Scattering, Collagen Density and Menopausal Status

To determine how these scattering differences might affect optical contrast in patients of different breast compositions, scattering was compared across sites with low and high percentage collagen as well as pre and post-menopausal status as a binary surrogate for age. Menopausal status was used because it was highly correlated with age (r=0.75). Scattering was found to be significantly lower in benign sites with low percentage of collagen in post-menopausal women compared to benign sites with a high percentage of collagen pre-menopausal women (unadj. p=5.3e-6) as would be expected. However, unexpectedly, benign sites with a high percentage of collagen in post-menopausal women were not statistically different from those with low percentage collagen in either pre- or post-menopausal women. These sites from post-menopausal women with high percentage of collagen were statistically lower than that of sites from pre-menopausal women with a high percentage of collagen (unadj. p=1.4e-4).
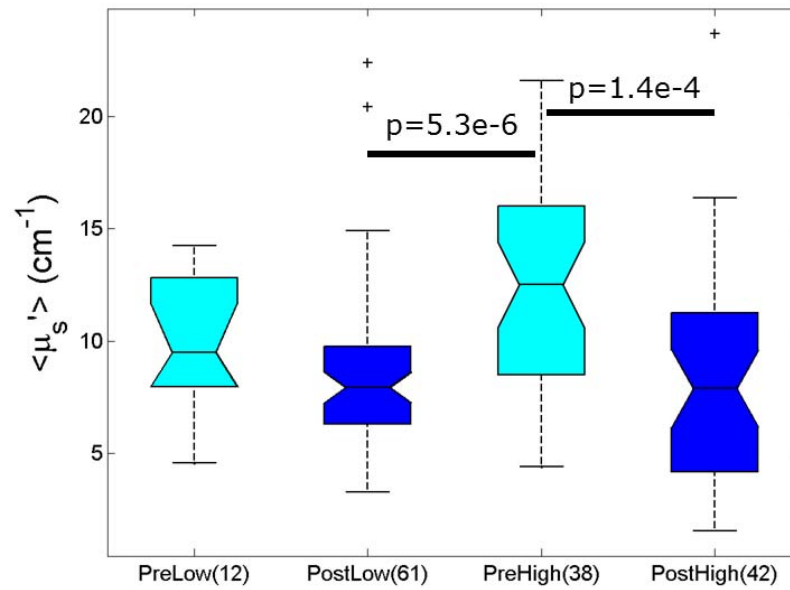
Figure 1.10: Sites from post-menopausal patients with low and high percentages of collagen exhibited the lowest scattering values. High collagen sites from pre-menopausal patients exhibited the highest scattering values. The difference in <μs′> values for malignant and benign sites would be greater in post-menopausal patients.

Relative Contributions of Collagen vs. Glands to Scattering

Lastly, the relationship between percent collagen and percent glands in benign, malignant, and all sites was analyzed to determine the relative contributions of stroma vs. epithelium to $<\mu_s′>$. The relationships between $<\mu_s′>$, the percent collagen and percent glands are shown in Table 1.5 in order to determine the contribution of collagen and glands to $<\mu_s′>$ respectively.

Table 1.5: Examining the dynamic range of the data include restricting sites to % glands <40%. Here, the % glands and % collagen were found to independently contribute to $<\mu_s′>$ in both benign and malignant sites. $<\mu_s′>$ increased with both collagen and glands; $<\mu_s′>$ exhibited a stronger positive relationship to glands in malignant sites.

$<\mu_s′>$ (cm^{-1})	Benign (n=85)		Malignant (n=18)		All (103)	
	R	p	r	p	r	P
%Glands	0.18	0.09	0.64	0.005	0.25	0.01
%Collagen	0.17	0.13	0.52	0.03	0.23	0.02

The linear models (Table 1.5) identified that both percent collagen and percent glands were independently associated with $<\mu_s′>$ in all sites and sites with glands (FG, Mix and Mal). The analysis of collagen vs. glands was narrowed to investigate sites with glands between 0-40% (the dynamic range of the data). The linear model reflected an equivalent relationship to scattering from percent glands and the percent collagen in benign sites (r=0.18 vs. r=0.17). In

addition, the malignant sites showed a slightly stronger positive relationship of percent glands (r=0.64, p=0.005) to $<\mu_s'>$ compared to the collagen content and $<\mu_s'>$ (r=0.52, p=0.03).
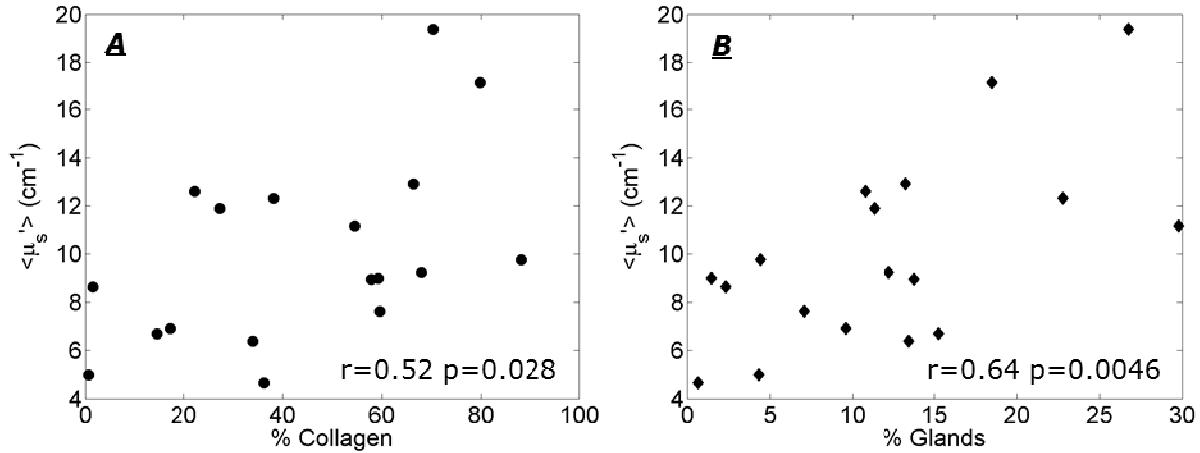

Figure 1.11: Statistical modeling was used to determine that both % collagen and % glands independently related to scattering in a positive direction with no relationship to one another. The relationship between scattering (A) % collagen and (B) % glands in malignant sites demonstrated a slightly stronger dependence upon glands.

The surgery, optical measurements and the histological processing of the tissue are described in detail elsewhere [20]. A total of 38 malignant sites and 595 benign sites from the previous study were examined for this analysis. These corresponding H&E slides for each of these sites were requested from Pathology. Each H&E slide was imaged, quantified and classified to determine the proportion of glands, collagen, adipose tissues as well as the size and density of adipocytes in predominantly fatty tissues.

c. Algorithm Development:

Impact of Scattering Model on Extracted Optical Properties:
The ability to gain insight into disease state based on the tissue's optical properties ultimately requires accurate extraction of those properties. Accurate extraction, in turn, requires that the assumptions made while modeling the tissue are valid. The inverse Monte Carlo method we employ to extract optical properties from the tissue requires knowledge of the functional form of wavelength-dependent scattering in the tissue as well as the wavelength-dependent spectra of each absorber present in the tissue (Hb, HbO2, β-carotene, and patent blue dye). Since each of the absorption spectra are known, the only assumption necessary to make about the tissue is the form of wavelength-dependent scattering. To date, we have assumed that scatterers in tissue can be modeled as spherical particles of a single size using Mie theory [11, 15, 16]. Clearly, however, cellular scatterers are neither spherical, nor of a single size. To ensure that modeling artifacts were not altering our extracted optical properties, we tested an alternative model for cellular scattering – the power law model. Several groups have shown that the wavelength-dependent scattering from a distribution of biological scatterers can be well

described using a power law: $\mu'_s = A\lambda^{-b}$, where A is a scaling constant, and b =(0.37, 4) [21]. Therefore, we compared the extracted optical properties from site-level data when using either a Mie model or a power law model to describe the wavelength dependence of tissue scattering.

Methods:

To perform this analysis, we compared the optical properties extracted from spectra from 64 sites in 56 patients whose patholoigist-determined compositions included: fibroglandular (n=3), adipose (n=49), fibroadipose (n=6), and malignant (n=6) tissues. Two inversions were performed: one using the standard Mie model assumption of a single scatter size whose diameter as between 350 nm and 1.5 µm, and the other assuming a power law distribution allowing b to be chosen in the range of 0.37 to 4.

Results:

Boxplots of the extracted optical properties ([β-carotene], <µs'>, [β-carotene], /<µs'>, [Hb] and [HbO]) are shown in Figure 1.12. The extracted values for all optical endpoints are nearly identical in the two analyses. This data suggests that the choice of scattering model has minimal effect on our Monte Carlo inversions. Therefore, we are confident that the optical properties extracted by our Monte Carlo model provide a sufficient description of the tissue and can be relied upon for discriminating between cancerous and benign tissue.
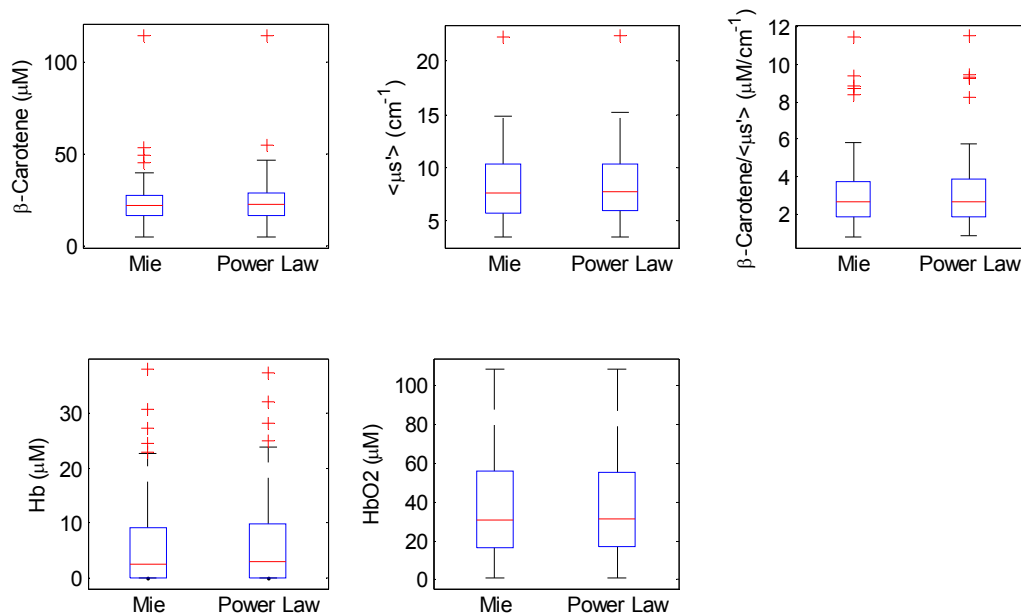
Figure 1.12: Box plots of the optical properties ([β-carotene], <µs'>, [β-carotene], /<µs'>, [Hb] and [HbO]) extracted from 64 fibroglangular, fibroadipose, adipose, and malignant sites. Properties were extracted with an inverse Monte Carlo model employing either a Mie model or a power law model for the wavelength dependence of scattering. The plots of all parameters suggest that the functional form of wavelength-dependent scattering does not change the extracted optical properties.

d. Clinical Study on Margin Assessment:

We have completed the development of the 49-channel imaging device which allows for faster acquisition of wide-field spectral images. To date, we have acquired images using the 49-channel system in 54 patients undergoing partial mastectomy, mastectomy or reduction mammoplasty. Of these samples, 29 have been imaged by the high resolution microendoscope. The goal of this imaging protocol is to use wide field spectral imaging of the entire margin followed by high resolution fluorescence interrogation of optically identified suspicious sites.

Software has been developed to invert the diffuse reflectance spectra from the 49-channel system and create optical parameter maps corresponding to the probe geometry using the previously detailed Monte Carlo inversion algorithm [11, 15, 16] (with the Mie model for scattering).   The software uses both the diffuse reflectance data and the model fits to process the images, discarding any pixels that were not in contact with tissue or resulted in poor fitting. To date, we have acquired images using the 49-channel system in 54 patients undergoing partial mastectomy, mastectomy or reduction mammoplasty. Of these samples, 18 were imaged using the final 49-channel probe design and have been analyzed. The rest of the images were excluded from analysis because they were acquired using an unoptimized probe. An example of an analyzed margin can be found in Figure 1.13. This sample image was of a small specimen located under the upper left corner of the 49-channel probe. Note that the processing algorithm discards spectra that lack the characteristic absorption features of β-carotene and hemoglobin. The processing algorithm also scales the values of the parameter maps based on the 10th and 90th percentiles of the extracted [β-carotene], /$<\mu_s'>$ values for the whole data set.
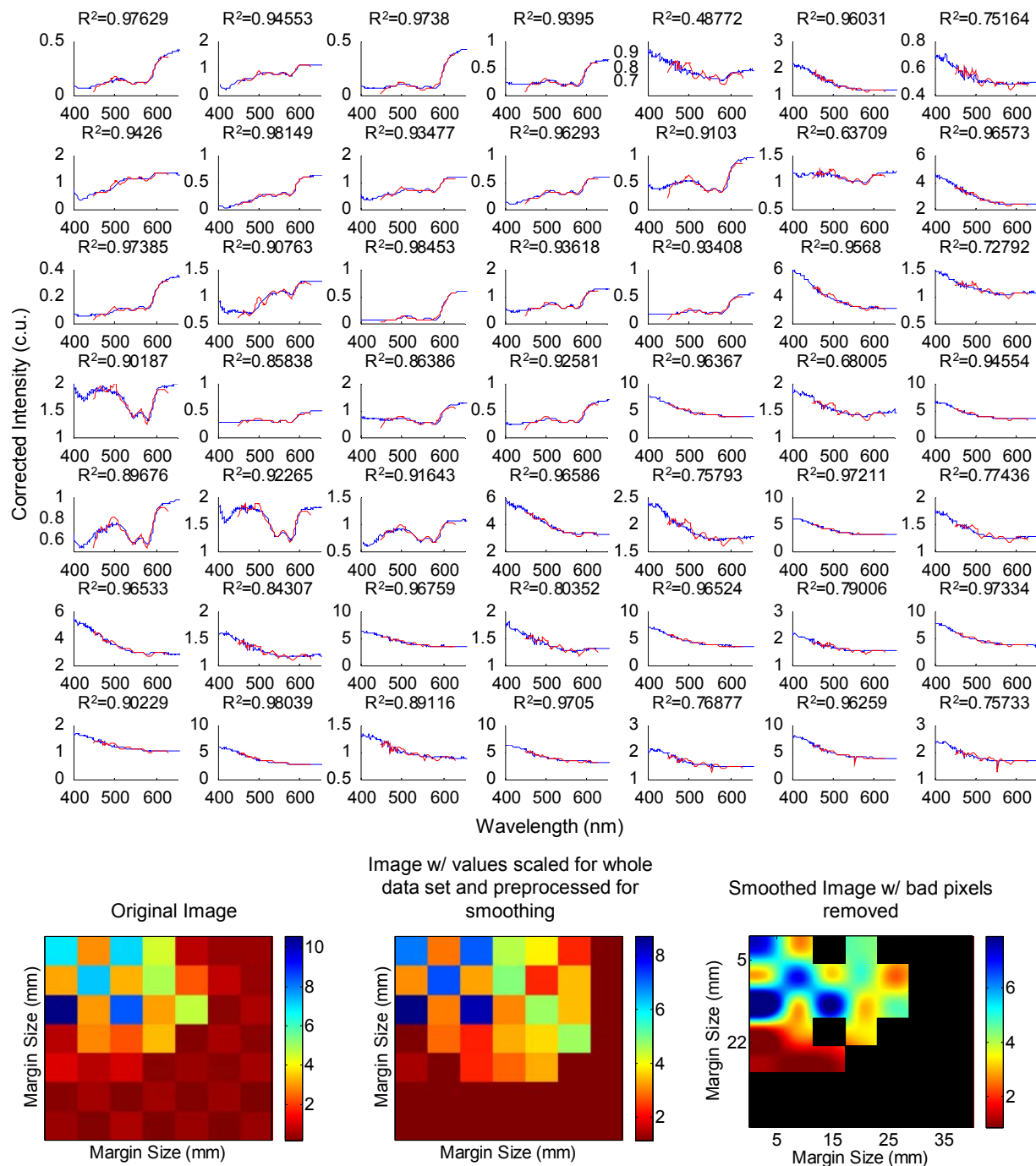
Figure 1.13: A sample image from the 49-channel probe of a small lumpectomy under the upper left corner of the imaging face. The top figure shows the diffuse reflectance spectra (blue) of each channel with its corresponding model fit (red) and goodness-of-fit parameter, R^2. These fits result in the original [β-carotene], $/<\mu_s'>$ parameter map (bottom left). Our custom software scales the image to the 10th to 90th percentiles of [β-carotene], $/<\mu_s'>$ extracted from all sites over the whole data set and preprocesses the image for smoothing (bottom center). Finally, the parameter map is smoothed and pixels with poor fits or non-contact spectra are eliminated (bottom right).

Plans for year 4:
In year 4, we will continue recruiting patients for the imaging protocol and will determine if the high resolution device enhances that ability to detect surgical margin status at time of surgery. We have amended our protocol to allow us to obtain pathology from mammoplasty specimens in order to fully understand the spectral and morphological contrast associated with all tissue types.

Aim 2: Optical quantitative biology of different breast cancer subtypes.
The objective of the work in Aim 2 is to use optical techniques to measure markers of the tumor microenvironment in women with cancers representing a wide variety of subtypes, and to determine whether these optical measures can be used for real time diagnosis or to predict eventual chemotherapy response in a subset of the patients who are measured prior to commencement of chemotherapy. One such approach that we have discussed in previous years is to use a high resolution microendoscope (HRME) combined with a morphological stain called acriflavine to visualize the tissue morphology in real time. Last year we demonstrated the feasibility of using the HRME for detection of residual carcinoma in the normal tissue milieu and validated our unique image analysis approach on preclinical murine tumor margin specimens and small cohort of clinical mastectomy samples. Here we focus primarily on image analysis techniques and our quantitative approach for diagnosing HRME images of heterogeneous breast tissue acquired from biopsy specimens. In Year 3, we have completed a large study using HRME to capture morphologically based information from biopsy specimens, and have identified several quantitative endpoints that can distinguish malignant from benign tissues.

Optical microscopy is a powerful technique to obtain high-resolution images of tissue histology in real-time at the point-of-care, without the need for fixing, sectioning, and staining. Various optical microscopy techniques including reflectance and fluorescence[12, 22, 23], Raman[24], confocal[25, 26], and optical coherence tomography[27, 28] have been used to exploit intrinsic sources of contrast in thick tissues. Additionally, fluorescence microscopy has been combined with vital fluorescent stains such as acridine orange (AO)[29-31], acriflavine[32, 33], and DAPI[34] to visualize micro-anatomical features in skin[29], breast[34], ovarian[31], oral[32], and esophageal[33] cancers. All of these technologies enable rapid and completely non-destructive visualization of tissue histology.

Robust methods for segmentation and quantitative analysis are essential to enable automated and rapid surveillance of tissue pathology, particularly when images are collected in near real time. Most approaches within the microscopy community depend on subjective observer interpretation[29, 30], gray level intensity information[33] or setting a threshold at a particular intensity level to isolate features of interest[34]. However, these simple image processing schemes have limited utility in thick tissues that exhibit a high degree of non-uniform background heterogeneity, such as is the case in the breast. To address this important need, we have developed computational technique that leverages morphologic information inherent in monochrome images of fluorescently-stained microanatomy to separate and quantify the presence of distinct tissue types in a heterogeneous image.

More specifically, the model based approach uses a heuristic analysis of tissue microanatomy to decompose tissue histology images into mathematically discrete components. First, a technique called sparse component analysis (SCA)[35], is used to separate cell nuclei, fibrous components, and adipose components, and second, the circle transform (CT) is applied to the deconstructed image to quantify the size and density of overlapping features of interest, in this case, nuclei as a means to identify the presence of disease in a biopsy specimen. Unlike other image processing techniques (such as watershed analysis, simple intensity thresholding, and frequency content analysis) the strategy described here does not rely heavily on intensity information, which can be compromised by excess background signal or calibration errors and does not represent a blind frequency analysis of the image content. More importantly this technique does not discard image content but rather retains all of the image information inherent in the image to preserve spatial relationships between tissue types, which is essential for proper interpretation of the images.

Methods:

Imaging system and contrast agent: A fluorescence microendoscope device that has previously been described in detail[32] was used to collect images of acriflavine stained tissues. The system contained a 455 nm light emitting diode (Luxeon V Star, LXHL-LR5C), excitation filter (Semrock, FF01-452/45-25) dichroic mirror (Chroma 485 DCLP), emission filter (Semrock, FF01-550/88-25), CCD camera (Point Grey Research, GRAS-14S5), and coherent fiber bundle (Sumitomo, IGN-08/30). The fiber bundle was composed of 30,000 fibers giving a circular field of view of approximately 750 µm in diameter. The resolution of the system was 4.4 µm. Images were produced by placing the fiber bundle in contact with the acriflavine stained tissue surface. Acriflavine (0.01% w/v, Sigma-Aldrich) dissolved in phosphate buffered saline (PBS) was topically applied to all specimens immediately prior to imaging.

Imaging protocol: The imaging protocol is illustrated in Figure 2.1. Patients undergoing a biopsy procedure at Duke University were consented. After the biopsy was removed from the patient, acriflavine was applied to the surface of the specimen. The distal end of the HRME fiber bundle was placed in contact with the tissue and images were acquired. The biopsy was scanned length-wise by systematically moving the probe in 1 mm increments over the tissue surface. Once one side was scanned, the biopsy was rotated 180 degrees and the length-wise scanning process was repeated. In order to improve the accuracy and reproducibility of these movements the fiber bundle was secured in a custom probe holder fiber chuck which was mounted on an x-y translation stage. Between each probe placement the distal end of the probe was cleaned with 55% ethanol.

Pathologic co-registration: After the imaging session the surface of the specimen was inked for pathologic co-registration. In order to maintain the proper orientation of the specimen for pathological evaluation, each end was inked with a different color. After imaging and inking was complete, the tissue was returned for standard pathologic processing, and the resulting hematoxylin and eosin (H&E) stained slides were reviewed by an expert oncology pathologist who was blinded to the results of HRME imaging. A diagnosis for each end of the biopsy as well as a diagnosis for the middle portion of the biopsy was given.
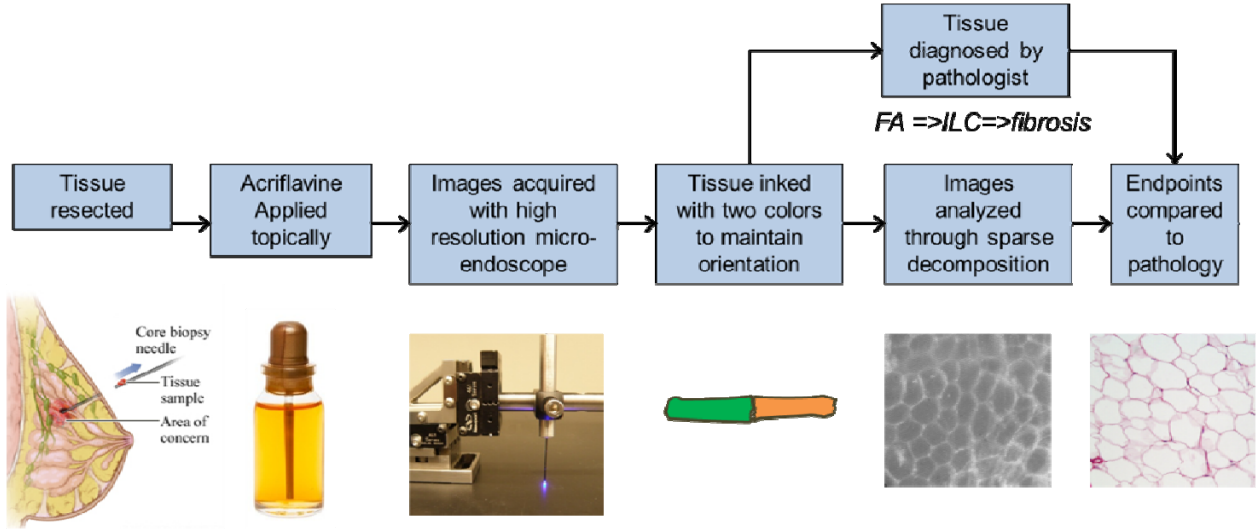
Figure 2.1: Diagram of biopsy protocol.

Image analysis. Since the most clinically relevant goal is to detect the presence of microscopic disease, we focused our quantitative approach on first isolating features of interest, such as nuclei, and then calculating features that may be used to determine the presence of tumor cells in an image, such as the size and density of those nuclei. Our first step was to remove the fiber core pattern that is superimposed onto each image (since the images are discretely sampled through a fiber bundle) by applying a Gaussian filter to remove the high frequency content. This step smoothed the image without removing spatial frequency information inherent to the tissue structure, and was done in order to remove the bias or artifact that the fiber pattern could introduce during subsequent image processing.

Next, in order to isolate the cell nuclei from other structures, such as muscle fibers/fibrous tissue or adipocytes, tissue components (nuclei, muscle fibers/fibrous tissue, and the outline of adipose cells) were separated computationally using a sparse decomposition analysis (SD) method. Let *y* denote the preprocessed image data, modeled as

$$y = x_{nuclei} + x_{muscle} + x_{adipose} + w \qquad (1)$$

Where x_{nuclei}, x_{muscle}, and $x_{adipose}$ denote the true nuclei, muscle/fibrous, and adipose components respectively, and *w* accounts for noise and small deviations from the model. The key assumption was that each tissue component has a different "sparsifying" basis or dictionary in which the expansion coefficients were nearly all zero, with only a few large coefficients. (For instance, an image of muscle fibers was relatively smooth, so it could be accurately approximated using a superposition of a small number of Fourier basis functions.) If the sparsifying dictionaries were sufficiently dissimilar, then the sparsity could be exploited to uniquely identify the different tissue components.

The pixel basis was used for the nuclei dictionary to capture the small and spatially isolated nuclei. The discrete cosine transform (DCT), a variant of the Fourier transform, basis was used to describe muscle components or fibrous content with periodic fiber structures. Mathematically

$x_{muscle} = F\theta_{muscle}$, where F was a matrix representation of the DCT, and θ_{muscle} was a vector of the DCT coefficients; most elements θ_{muscle} of were zero. The curvelet dictionary was used to represent the curvilinear outlines of adipose cells[36]. Curvelets, similar to wavelets, had dictionary elements corresponding to different scales and locations throughout an image and were relatively dissimilar to both the pixel and DCT bases[36]. Let C denote the curvelet transform matrix so that $x_{adipose} = C\theta_{adipose}$, where $\theta_{adipose}$ was a sparse curvelet coefficient vector.

The sparse coefficient vectors were estimated by solving a regularized least-squares inversion[15]:

$$\left(\hat{x}_{\text{nuclei}}, \hat{\theta}_{\text{muscle}}, \hat{\theta}_{\text{adipose}}\right) = \underset{x_{\text{nuclei}}, \theta_{\text{muscle}}, \theta_{\text{adipose}}}{\operatorname{argmin}} \quad \tfrac{1}{2}\left\| y - (x_{\text{nuclei}} + F\theta_{\text{muscle}} + C\theta_{\text{adipose}}) \right\|_2^2$$

$$+ \tau_{\text{nuclei}} \left\| x_{\text{nuclei}} \right\|_1 + \tau_{\text{muscle}} \left\| \theta_{\text{muscle}} \right\|_1 + \tau_{\text{adipose}} \left\| \theta_{\text{adipose}} \right\|_1$$

$$\hat{x}_{\text{muscle}} = F\hat{\theta}_{\text{muscle}}$$

$$\hat{x}_{\text{adipose}} = C\hat{\theta}_{\text{adipose}}$$

$$\hat{x}_{\text{approx}} = \hat{x}_{\text{nuclei}} + \hat{x}_{\text{muscle}} + \hat{x}_{\text{adipose}} \tag{2}$$

Where the argmin element returned the value of the argument that minimized the l_2 and l_1 norms. The l_2 term in Eqn. 2 ensured that the approximation $\hat{x}_{approx}$ was a good fit to the observed data, while the l_1 terms promoted sparsity in the variables x_{nuclei}, θ_{muscle}, and $\theta_{adipose}$. The regularization parameters τ_{nuclei}, τ_{muscle}, and $\tau_{adipose}$ were positive weights that controlled the balance between data fidelity and sparsity in the reconstruction. These parameters were selected using an empirical method described in the supplementary methods. To solve this minimization problem, the Gradient Projection for Sparse Reconstruction (GPSR) algorithm was used[37]. After SD was applied to isolate nuclei, the nuclear size and density were quantified by computing the circle transform on $\hat{x}_{nuclei}$ to detect approximately circular objects (*i.e.*, nuclei). An illustration of the sparse decomposition algorithm applied to image containing adipose cells with nuclei scattered throughout is shown in Figure 2.2. In this example the DCT image is black because there is no muscle or fibrous tissue present in the original image.
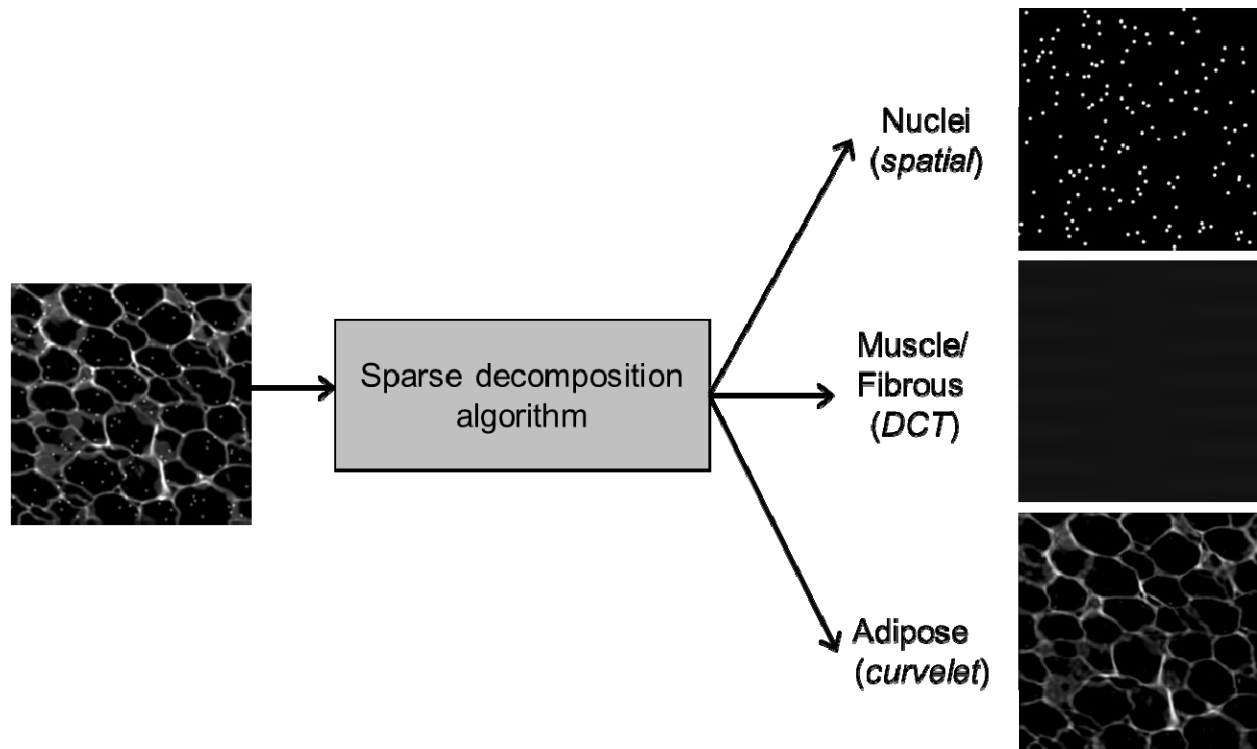
Figure 2.2: Sparse decomposition illustration. An image containing adipose cells with nuclei scattered throughout can be separated into its constituents through the sparse decomposition algorithm. The spatial image captures the randomly distributed nuclei, while the DCT image describes the periodic muscle components and the curvelet image captures the curved outline of adipose cells. In this example the DCT image is black because there is no muscle or fibrous tissue present in the original image.

Statistical analysis: Wilcoxon rank sums (non-parametric, two-tailed, alpha = 0.95) were used to determine whether quantitative image parameters were significantly different between biopsies that contained malignant tissue versus those that contained only benign tissue. A significance level of $p < 0.05$ was considered to reject the null hypothesis for all analyses. The n for each statistical analysis is listed in the respective figure label.

Results:

The breakdown of biopsies specimens imaged in this study is shown in Figure 2.3. We consented 47 patients and were able to image 44 biopsy specimens (we had 3 screen fails for various reasons). We currently have received a pathology diagnosis for 42 of the 44 (2 pathology report are pending at this time). Within the 42, we have 19 malignant and 23 benign specimens. The 19 malignant are comprised of 13 invasive ductal carcinomas (IDC), 2 invasive lobular carcinomas (ILC), 3 ductal carcinomas in situ (DCIS), and 1 that contains both IDC and DCIS. Of the 23 benign biopsies, 19 contain some combination of fibrous and fat tissue. The remaining 4 benign biopsies are either fibroadenomas, papillomas, of fibrocystic change (FCC).
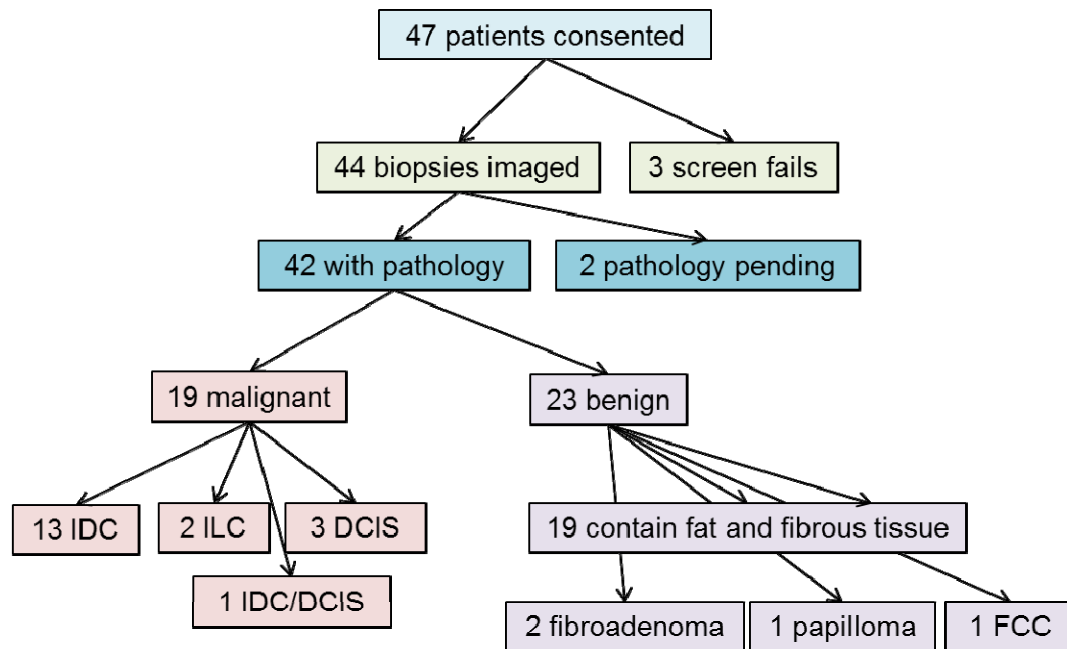
Figure 2.3: Breakdown of biopsy specimens.

Figure 2.4 shows a representative example of one of the malignant biopsies from our study. As described in the methods each side was scanned length-wise—side 1 corresponds to the top row and side 2 corresponds to the bottom row. In this example, the left hand side contains IDC, the middle contains IDC and fibrous tissue, and the right hand side contains fat tissue and inflammation. As seen, large round cells, characteristic of adipose tissue, can be seen on the right hand side, while the rest of the panel is filled with a random distribution of disorganized nuclei, which is characteristic of IDC. The outputs from sparse decomposition are shown in (B) though (D). As seen in (B), many nuclei are present throughout the panel. Both (C) and (D) contain elements of the background. While the DCT component (C) is meant to isolate only fibrous or muscle structures, any periodic pattern within the image is captured here. Similarly, while the curvelet component (D) is meant to isolate only the outline of adipose cells, any curvilinear structure within the image is captured here. While this algorithm does not perfectly capture or separate out the fibrous and adipose components, it is able to effectively isolate nuclei, which can be very diagnostically informative as is discussed below.
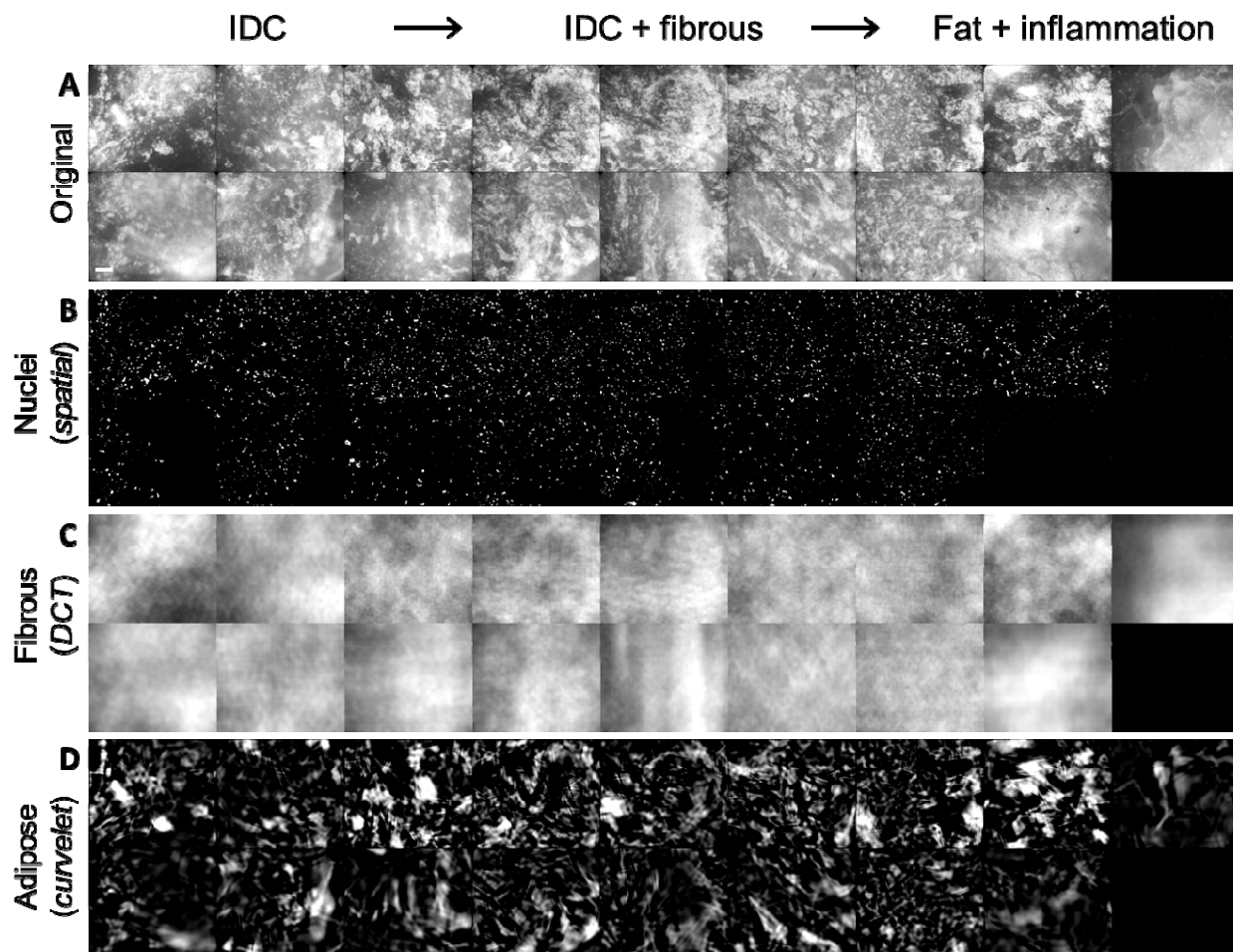
Figure 2.4: Sparse decomposition applied to a representative malignant biopsy containing IDC. Both sides of the biopsy we scanned length-wise resulting in the two rows in (A). The pathological diagnosis was given for the left end (IDC), middle (IDC + fibrous tissue), and right end (Fat + inflammation) respectively. The outputs from sparse decomposition are shown in (B) – (D). (B) shows nuclei isolated in the spatial bin, while (C) shows periodic features isolated in the DCT bin, and (D) shows curvilinear features isolated in the curvelet bin.

Similarly, Figure 2.5 shows a representative benign biopsy from our study. In this example, the left hand side contains fibroadipose tissue (FA), the middle contains fibroglandular (FG) and fat tissue, and the right hand side contains fat tissue. As seen, large round cells interspersed with string-like fibrous tissue, characteristic of fibroadipose tissue, can be seen on the left hand side, while the middle and right hand side of the panel contains primarily adipose and less fibrous tissue. The outputs from sparse decomposition are shown in (B) though (D). As seen in (B), nuclei that are located on the periphery of the adipose cells are isolated throughout the panel. Both (C) and (D) contain elements of the background. In particular, (D) contains some very bright areas where the curvilinear fibrous tissue that is interspersed throughout the adipocytes was isolated. More of these bright areas are seen on the left hand side of the panel, which contains more fibrous tissue.
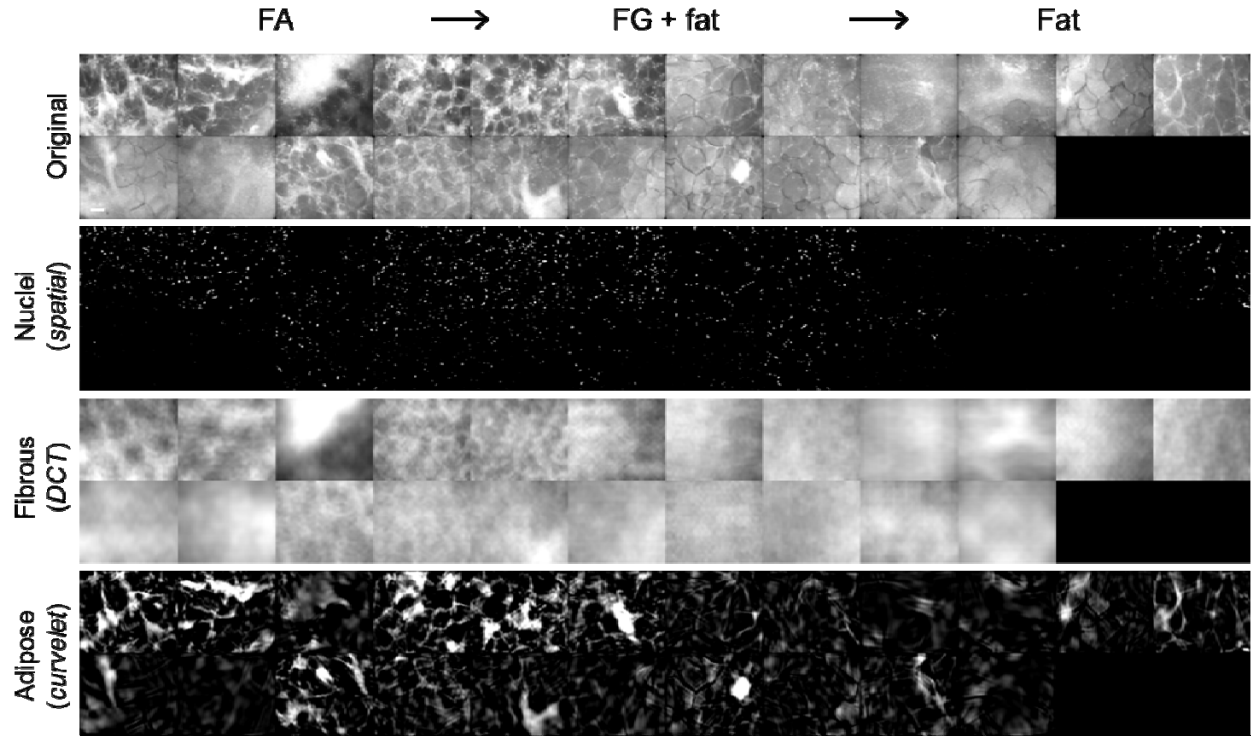
Figure 2.5: Sparse decomposition applied to a representative benign biopsy containing fat and fibrous tissues. Both sides of the biopsy we scanned length-wise resulting in the two rows in (A). The pathological diagnosis was given for the left end (FA), middle (FG + fat tissue), and right end (Fat tissue) respectively. The outputs from sparse decomposition are shown in (B) – (D). (B) shows nuclei isolated in the spatial bin, while (C) shows periodic features isolated in the DCT bin, and (D) shows curvilinear features isolated in the curvelet bin.

After obtaining the outputs from the sparse decomposition algorithm, we sought to calculate parameters, such as the density of nuclei, which could have diagnostic potential. An illustration of our quantitative approach is shown in Figure 2.6. For each biopsy, the images with the two highest densities were identified, which is delineated by the red boxes in both (A) and (D). Next, nuclei greater than 8 μm in diameter were false colored red and nuclei less than 8 μm in diameter were false colored green and overlaid onto the curvelet output, which is shown in (B) – (F). This approach was taken to illustrate that the information present in the DCT and curvelet images can be used to determine whether nuclei are associated with normal tissue (for example if a nucleus is located on the periphery of a skeletal muscle fiber or adipocyte in which case the nuclei are most likely benign and part of a normal tissue architecture), or whether the nuclei are in isolation and not associated with normal stromal morphology, in which case a nucleus is more likely to be associated with disease. In particular, in (E) and (F) most of the nuclei are spatially co-registered with the outline of an adipocyte, while there is no clear association between the nuclei and the curvilinear features in (B) and (C), which contain IDC.
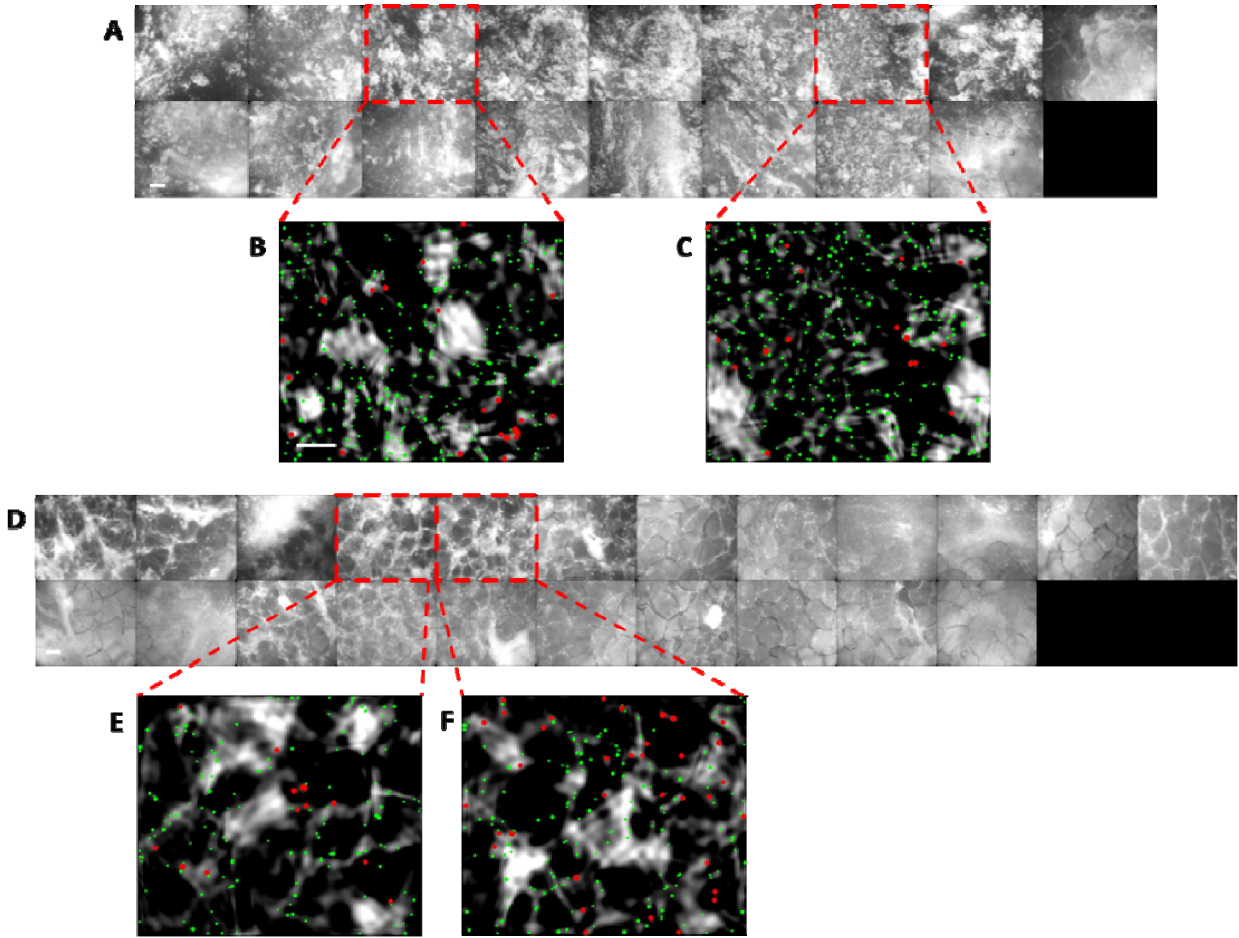
Figure 2.6: Illustration of quantitative analysis applied to outputs obtained from sparse decomposition. For each biopsy, the images with the two highest densities were identified, which is delineated by the red boxes in both (A) and (D). (A) is a representative malignant biopsy containing IDC, which was shown in figure 2.4. (D) is a representative benign biopsy containing fat and fibrous tissue, which was showing in figure 2.5. Next, nuclei which were greater than 8 μm in diameter were false colored red while nuclei that were less than 8 μm in diameter were false colored green and overlaid onto the curvelet output, which is shown in (B) – (F). The max densities, curvelet intensities, and ratios between the max densities and curvelet intensities were quantified and shown in the next figure.

Next, the two highest densities within each panel, the associated curvelet intensities, and the ratios between the two highest densities and the associated curvelet intensities were quantified. The differences between the malignant and benign biopsies are shown in Figure 2.7 (A) – (C) respectively. P-values obtained from Wilcoxon rank sums are also shown in (A) – (C). The maximum densities present in malignant biopsies were significantly higher than the maximum densities seen in benign biopsies (p = 0.0046). The curvelet intensities present in these same images did not show significant differences between malignant and benign biopsies; however when ratios between the maximum densities and the curvelet intensities were calculated, the difference between malignant and benign biopsies was even more significant (p = 0.0026). This suggests that combining variables may be better able to distinguish biopsies that contain disease from those that do not. The malignant variants were then further stratified into IDC,

DCIS, and ILC, and the benign variants were further stratified into fat/fibrous (Fat/Fib) and fibroadenoma/papilloma/fibrocystic change (Other) for the same parameters and are shown in (D) – (F) respectively. As seen, biopsies with IDC have (on average) the highest densities, followed by ILC, DCIS, other, and Fat/Fib. However, it is interesting to note that the densities in DCIS are very similar to the densities seen in some of the normal pathologies, which include fibroadenoma, papilloma, and fibrocystic change. This suggests that using a combination of multiple parameters may enable better discrimination between various pathologies.
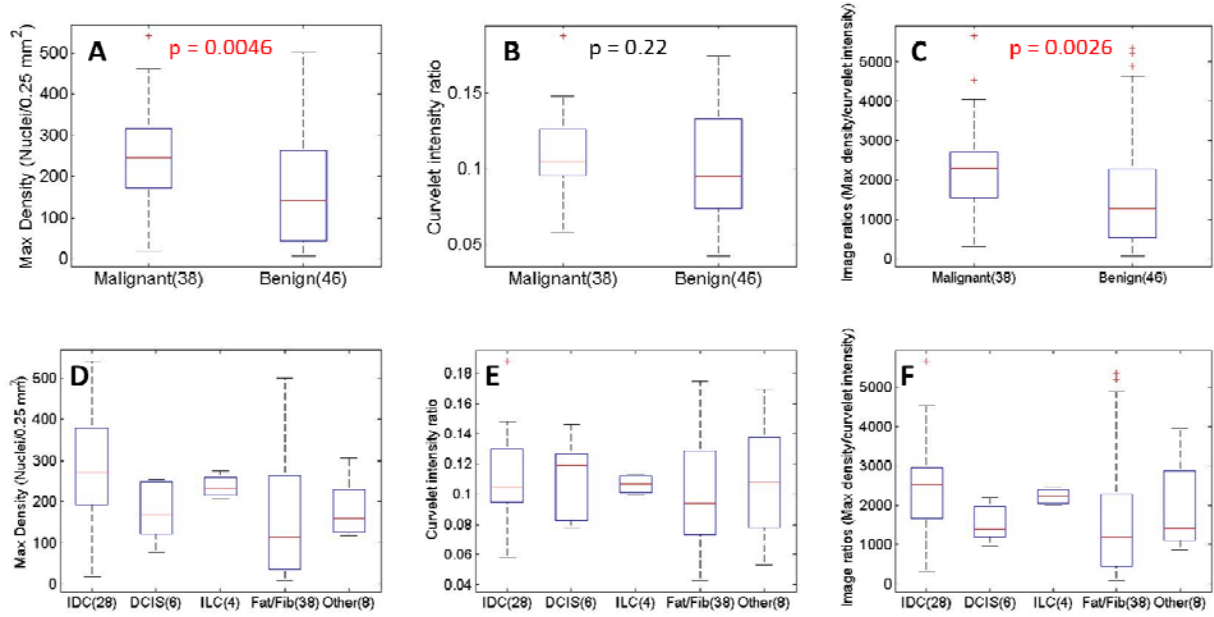

Figure 2.7: Quantification of parameters. The max densities, curvelet intensities, and ratios between the max densities and curvelet intensities were quantified and the differences between the malignant and benign biopsies are shown in (A) – (C) respectively. P-values obtained from Wilcoxon rank sums are also shown in (A) – (C). The malignant variants were then further stratified into IDC, DCIS, and ILC, and the benign variants were further stratified into fat/fibrous (Fat/Fib) and fibroadenoma/papilloma/fibrocystic change (Other) for the same parameters and are shown in (D) – (F) respectively.

In conclusion, high resolution fluorescence imaging of acriflavine stained tissue combined with an algorithm that leverages sparse decomposition analysis and circle transform (SD+CT) provides a rapid, non-destructive and automated strategy for quantitative pathology of thick tissues with non-uniform background heterogeneity. Unlike nuclear stains such as DAPI, acriflavine stains connective tissue, such as skeletal muscle, fibrous tissue, and the outline of adipose cells, in addition to nuclei. Thus in addition to being able to detect increased nuclear size and density, which are traditional hallmarks of carcinogenesis, it is also possible to place nuclei within the context of the entire histological landscape, which can further indicate whether a particular nucleus is associated with benign or malignant tissue[38, 39]. This provides a powerful alternative to complicated and time-intensive immunohistochemistry techniques, which require fixing, sectioning, and staining and which can only be performed on the excised margin.

In addition to our work at Duke University, our collaborators at Rice have been using the high resolution optical imaging to explore the correlation between morphologic biomarkers assessed from high resolution optical images (epithelial cell density and N/C ratio; collagen density, fiber size, fiber linearity; adipocyte size and density) and histologic diagnosis and biomarkers of cancer risk and progression. They acquired images from resected tumor and needle biopsy specimens. To date, they imaged a total of 126 specimens from 64 patients. Images were obtained using both a commercial laser scanning confocal device and the HRME described in the original proposal. These images were assembled into a library of normal, non-neoplastic features and neoplastic lesions to facilitate comparison between high resolution optical images and the corresponding histological sections. They identified a total of 235 sites with corresponding histological features in confocal images and images prepared using standard histologic preparation. Figure 2.8 shows examples of image pairs for 3 histological categories.
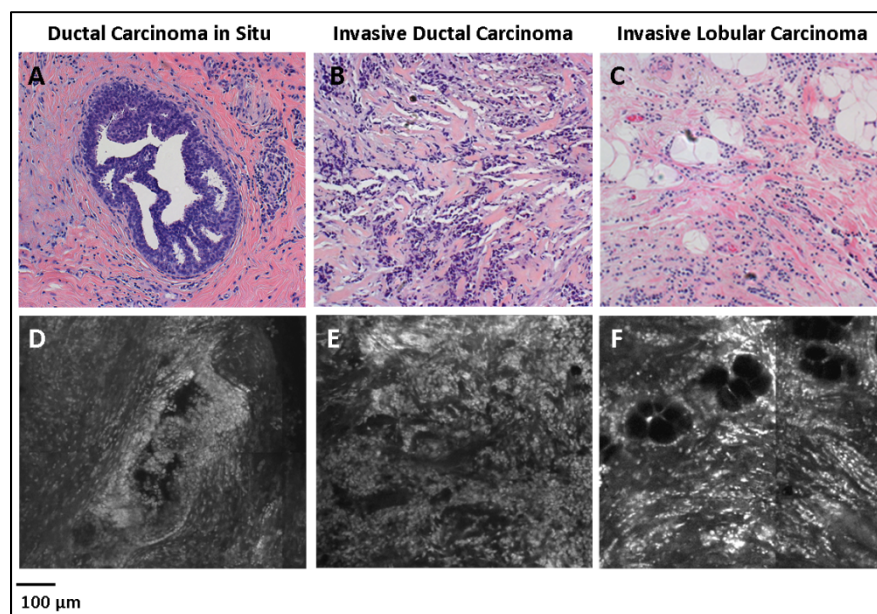

Figure 2.8: Corresponding sites in neoplastic lesions imaged using standard histologic preparation (A-C) and confocal fluorescence microscopy (D-F). Ductal carcinoma in situ is identified as an abnormal increase in cell number, resulting in crowding and disorganization within the duct (A, D). Invasive ductal carcinoma is characterized as malignant cells which have invaded outside of a duct into the surrounding stroma (B,E) . Invasive lobular carcinoma is characterized by cells invading in a single file line (C,F).

The images in the library have been organized into a training set and a validation set to test the accuracy of confocal fluorescence microscopy compared to the reference standard, histologic assessment. The training set will be used to demonstrate to readers how to evaluate confocal images of normal, benign, and malignant breast features. The validation set will be used to test sensitivity and specificity of confocal fluorescence microscopy for assessment of breast lesions. Rice will test for sensitivity and specificity using qualitative visual impression as well as quantitative analysis. Two pathologists associated with the study have assessed the validation sets and analyzed histology and confocal fluorescence microscopy by visual impression. Table 2.1 shows the sensitivity and specificity of visual impression for analysis of histology with H&E staining and confocal fluorescence microscopy. Figure 2.9 shows the ROC curve for these data.

	Histology with H&E	Confocal Fluorescence Microscopy
Sensitivity (±SD)	100% (±0%)	95% (±7%)
Specificity (±SD)	95% (±3%)	95% (±8%)

Table 2.1: Sensitivity and specificity of visual impression for analysis of histology and confocal fluorescence microscopy. Standard deviation (SD) is given for each value.
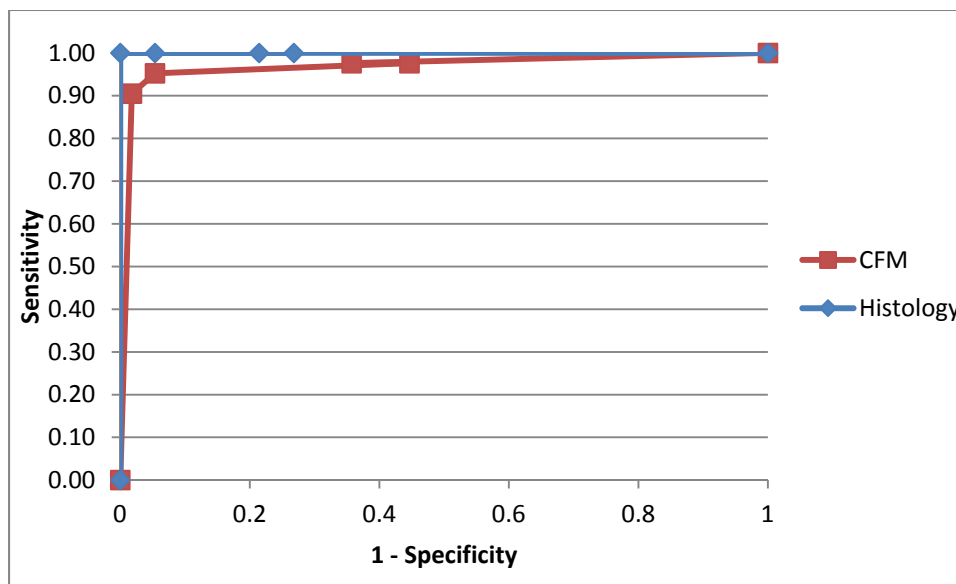

Figure 2.9: Receiver operating characteristic (ROC) curve describing the accuracy of confocal fluorescence microscopy (CFM) compared to standard histology.

Our collaborators have used the images in the library to begin quantitative evaluation of morphologic features, including adipocyte size and density. Our first analysis was performed using manual segmentation of adipocytes within normal adipose tissue, and at the boundary of invasive tumors and lesions of ductal carcinoma in situ. They manually segmented adipocytes in a total of 22 sites from 9 breast tissue specimens (Table 2.2). The preliminary results (Figure 2.10) suggested that adipocytes at invasive tumor boundaries were smaller in size compared to adipocytes within normal tissue and at the borders of in situ lesions. Figure 2.11 shows that, based on results from manual segmentation of adipocytes, the mean size of adipocytes adjacent to invasive ductal tumors is lower than the mean size of adipocytes adjacent to DCIS foci and in normal adipose tissue. We developed an algorithm to automate segmentation of adipocyte cells, which we are using to analyze a larger number of images of normal tissue, in situ lesions, and invasive lesions.
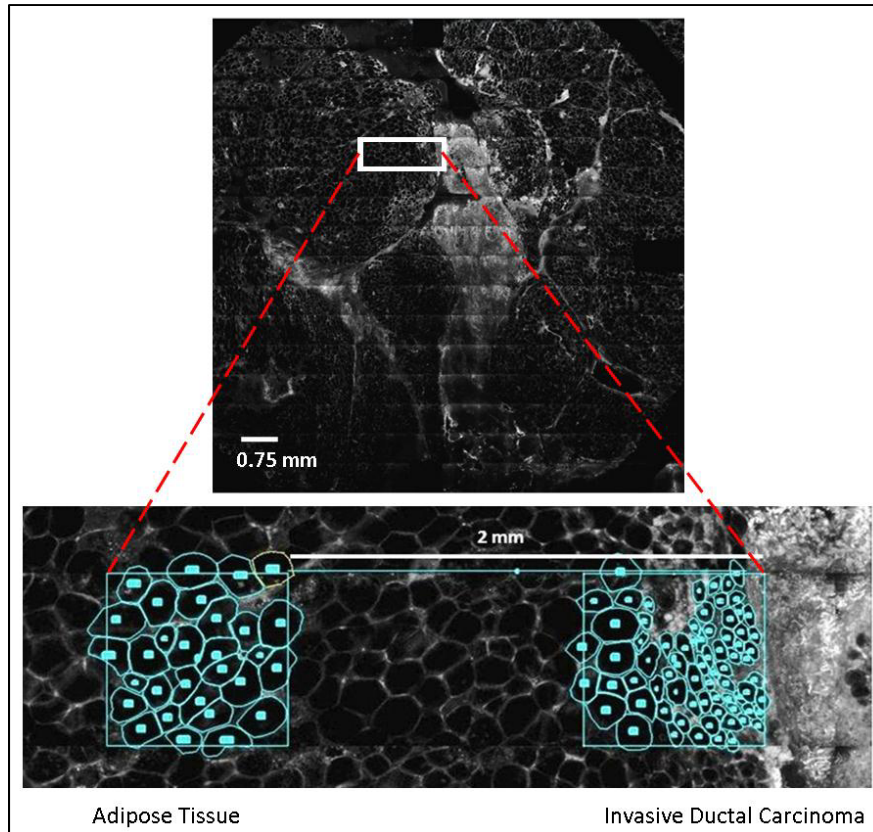
Figure 2.10: Manual segmentation of adipocytes adjacent to invasive ductal carcinoma imaged with confocal fluorescence microscopy. Sites were chosen at the boundary of the invasive lesion and in adipose tissue, 2 mm from the lesion boundary. Adipocytes within each region were traced manually and the size of each adipocyte was recorded.

	Specimens	Sites
Normal	4	8
DCIS	1	3
IDC	4	11
Total	9	22

Table 2.6: Summary of sites and specimens assessed using manual segmentation.

Figure 2.11: Mean adipocyte size measured in normal adipose tissue and adjacent to DCIS and IDC lesions acquired by manual segmentation. The columns indicate the mean adipocyte size in normal sites, sites adjacent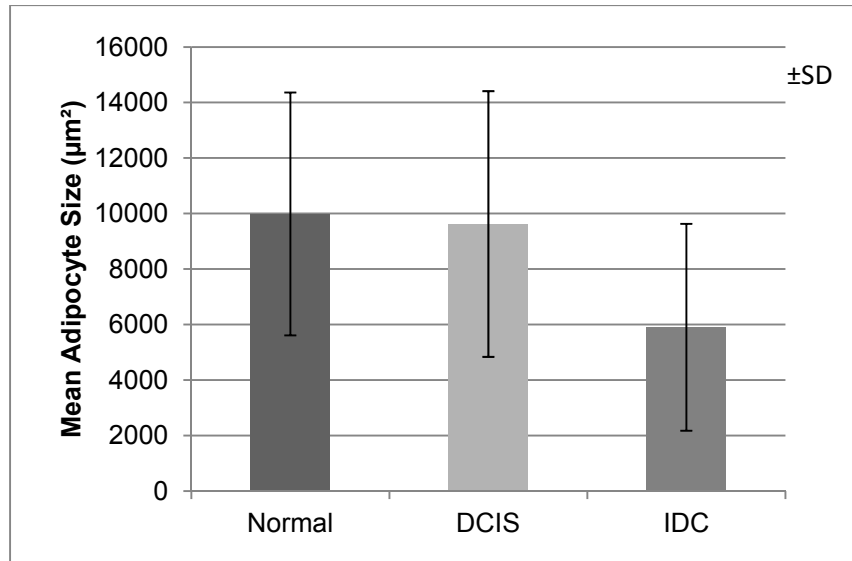 to DCIS, and sites located at invasive tumor boundaries. Error bars indicate positive and negative standard deviation (SD). The results show that the average adipocyte area in sites adjacent to IDC tumors differs from the average adipocyte size in sites of other histologies.

Plans for year 4:

Plans for year 4 include continuing to fine tuning this algorithm for clinical breast specimens, identifying additional endpoints/parameters that have diagnostic potential (such as the size of nuclei), and building predictive models that can quantitatively diagnose high resolution images in real time.

Rice University has three primary goals for the coming year:

- Develop tools to quantitatively analyze morphological biomarkers (such as epithelial cell density; collagen density, fiber size, fiber linearity) in high resolution optical images.
- Continue to explore the correlation between morphologic biomarkers assessed from high resolution optical images (epithelial cell density; collagen density, fiber size, fiber linearity) and histologic diagnosis and biomarkers of cancer risk and progression.
- Design fluorescent contrast agents specifically targeted to known biomarkers of breast cancer (such as Estrogen receptor, Progesterone receptor, HER2) and markers of inflammation (CD45), which can be imaged using high resolution optical imaging tools.

Aim 3: *Optical quantitative biology to assess therapy response in different sub-types of breast cancer:*

The currents goals of Aim 3 include the study of tumor metabolic and vascular response to stress in cell lines that were bound by a common theme – metastatic or non-metastatic, radiosensitive or radioresistant. In Year 3, we have made good progress towards achieving the goals stated in our previous report's Year 3 plans. First, we used a fluorescent glucose analog, 2-NBDG, to report on glucose uptake *in vitro* and *in vivo*. First, We used a hypoxic stress to perturb two murine mammary adenocarcinoma lines – 4T1 and 4T07. The 4T1 cell line is metastatic and forms robust secondary tumors in the liver and lung whereas the 4T07 is not capable of forming metastases. We measured the glucose uptake in both cell lines under normoxic conditions and in response to the hypoxic stress. Second, we studied the spatiotemporal relationship between vascular oxygen saturation and glucose uptake in 4T1 and 4T07 tumors grown in dorsal skin flap window chamber models. We are in the process of submitting these results for publication. Finally, we used optical spectroscopy to measure *in vivo* concentrations of 2-NBDG. Using validated algorithms that were rigorously tested on tissue simulating phantoms, we measured the vascular hemoglobin saturation and 2-NBDG concentration in flank tumors that received increasing doses of 2-NBDG. These results have been published recently in the Journal of Biomedical Optics.

Introduction:

The future of cancer management lies in the development of effective tumor-specific therapy. Every year, thousands of benign cancers such as ductal carcinoma in situ (DCIS) are managed the same way as more malignant forms of breast cancer. Efforts in the cancer community have been devoted to developing 'personalized medicine' by characterizing the genomic profiles of tumors. However, it is becoming evident that a single tumor can exhibit large spatial heterogeneities in genotype, making genomic profiling-based treatment a tough task [40]. Tumors of the same organ also differ in the hallmarks they exhibit, such as loss of function of tumor suppressors or gain of function of oncogenes. In spite of these variations in molecular events and signaling pathways, almost all cancers exhibit a common *phenotype* – increased glucose metabolism relative to normal cells [41]. Although the switch to glycolysis is mediated by hypoxia and hence, hypoxia-inducible factor (HIF) activity,[42] several tumors retain the same phenotype even in the presence of oxygen – a phenomenon first observed by Otto Warburg and hence named the Warburg effect or aerobic glycolysis [43].

One way to delineate Warbugian from Pasteurian tumors is to determine their responsiveness to hypoxic stress. Among human breast cancer lines, the MDA-MB-231 and MDA-MB-435 lines are known to be highly aggressive and metastatic relative to the slow-growing and benign MCF-7 line. *In vitro* studies have shown higher glucose uptake in MDA-MB-231 and 435 lines under normal oxygen conditions than the MCF-7 line. The glucose uptake of the metastatic cell lines is relatively unperturbed by hypoxic stresses, but hypoxia increases glucose uptake drastically inthe benign MCF-7 line [44, 45]. Therefore, a lack of correlation between glucose uptake and oxygenation could be indicative of the aggressive aerobic glycolysis phenotype.

Our long-term goal is to determine whether the oxygenation-metabolic demand relationship changes in a tumor in response to stress and whether this response or change can be indicative of long-term tumor behavior. In this report, we describe the steps we have taken to progress towards our goal and lay out our plan for the next year.

Methods:

In vitro cell culture

4T1 and 4T07 murine mammary adenocarcinoma lines were cultured in Dulbecco's Modified Eagle Medium (DMEM) supplemented with 10% fetal bovine serum (FBS) and 1% antibiotics. For imaging experiments, the cells were trypsinized and seeded on 60mm tissue culture plates 24 hours before imaging according to established protocols.

In vitro cycling hypoxia

An INVIVO$_2$ 500 hypoxia workstation (Ruskinn Technology Ltd, UK) was used for *in vitro* hypoxia perturbations. Cell plates were subjected to one hour of hypoxia followed by one hour of normoxia for a total of five hours (3 cycles of hypoxia and 2 cycles of normoxia). Imaging was performed immediately following the last hypoxic cycle.

In vitro multiphoton imaging

Prior to imaging, each cell plate was washed with phosphate buffered saline (PBS) and was incubated with 100µM 2-NBDG (in glucose-free DMEM). For the 2-NBDG retention and intermittent hypoxia experiments, cell plates were incubated for 20 minutes. For the 2-NBDG uptake kinectics experiment, plates were incubated from 1-75 minutes. Control plates were incubated with glucose-free DMEM containing no 2-NBDG for the corresponding time period. After incubation, each plate was washed once with PBS, refilled with PBS, and imaged immediately. All imaging was performed using the Olympus FV1000 Multiphoton microscope housed in the Duke University Light Microscopy Core Facility. 2-NBDG was excited at 960nm and emission was collected from 495-540nm.

Dorsal skin flap window chamber model

All *in vivo* experiments were conducted according to a protocol approved by Duke University Institutional Animal Care and Use Committee. We surgically implanted titanium window chambers on the back of female athymic nude mice (nu/nu, NCI, Frederic, Maryland) under anesthesia (i.p. administration of ketamine (100 mg/kg) and xylazine (10 mg/kg)). We injected a 20 µL suspension (20,000 cells) of 4T1-RFP or 4T07 cells into the dorsal skin fold and placed a glass coverslip (dia = 12 mm, No. 2, Erie Scientific, Portsmouth, New Hampshire) over the exposed tissue. In a separate group of control mice, we injected 20 µL of saline. All animals were housed in an on-site housing facility with *ad libitum* access to food and water and standard 12-hour light/dark cycles. A flowchart depicting the experiment protocol is presented in Figure 3.1. For baseline measurements, the animals were kept in a chamber filled with 21% oxygen for 6 hours. For cycling hypoxia, the animals were exposed to alternating 1-hour cycles of 21% oxygen and 10% oxygen for 6 hours. During this 6-hour period, the animals were only provided

with water. For *in vivo* studies alone, 4T1 cells were transduced by retroviral siRNA to constitutively express the red fluorescent protein (RFP) DsRed, allowing easy demarcation and growth tracking of tumor cells *in vivo*.
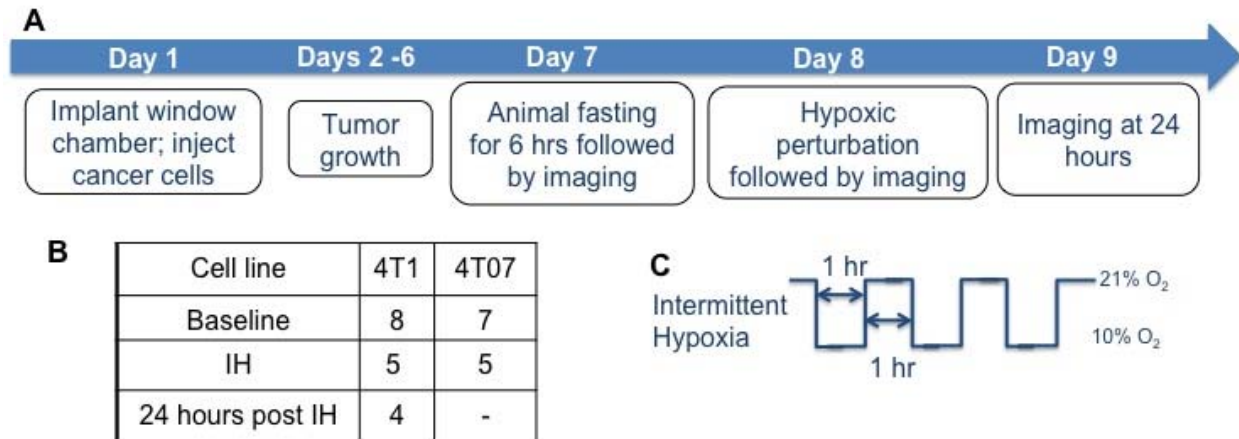

Figure 3.1: Experiment and 2-NBDG imaging protocol. A) Window chambers were surgically implanted in the dorsal skin flap of female nude mice. 4T1 or 4T07 cells were injected under the fascia below the chamber and allowed to grow for a week. Animals were fasted for 6 hours and injected with 2-NBDG to image the baseline glucose uptake and vascular saturation. 24 hours later, animals were subject to the hypoxia protocol and imaged again at the end. B) Sample size for the study. C) Illustration of hypoxia protocol.

Tumor xenograft model

Six to eight week old female athymic nude mice (nu/nu, NCI, Frederic, MD) weighing 25-30 g were used in these studies. Animals were housed in an on-site housing facility with ad libitum access to food and water and standard 12-h light/dark cycles. All animal experiments were conducted during the day and mice were fasted for 6 hours prior to optical measurements. Fasting ensured that glucose in the body did not compete with 2-NBDG uptake and good signal contrast from the tumor compared to normal tissue. Each mouse received a subcutaneous injection of 750,000 4T1-RFP cells in an injection volume of 100 μl. Flank tumors were monitored every other day and allowed to grow to a volume [$\pi/6$ x length x (breadth)^2] of 200 mm^3. A total of 7 tumor-bearing animals were divided into 3 groups and each group received 2, 4 or 6 mM of 2-NBDG (two animals in 2 mM group, three in 4mM group and three in 6 mM group). A volume of 100 μl of 2-NBDG was injected systemically through the tail-vein of the mouse.

Hyperspectral imaging of oxygen saturation and glucose uptake

We used a Zeiss Axioskop 2 microscope for recording all images. At the end of 6 hours of fasting, we initially recorded trans-illumination images, RFP fluorescence (for 4T1-RFP cells) and corresponding background images. In addition, a free space trans-illumination image using appropriate neutral density filters was recorded before every imaging session to account for daily variations in light intensity. The animals were administered a 100 μL tail-vein injection of 2-NBDG (6mM; MW: 342.16) dissolved in sterile saline. We recorded the 2-NBDG fluorescence

75 minutes as follows: Continuously for the first 8 minutes, every 30 seconds for the next 30 minutes and every 3 minutes for the final 35 minutes of imaging. A modified form of the Beer-Lambert law that describes absorption of chromophores in thin slices is fit to the trans-illumination image cube (x,y,λ) to obtain the concentration of the primary absorbers – oxy [O$_2$Hb] and deoxy-hemoglobin [dHb] at each pixel [46]. This is possible due to knowledge of the extinction coefficients of both absorbers. Based on this information, we can calculate total hemoglobin content [THb = O$_2$Hb + dHb] and oxygen saturation of hemoglobin [HbSat = O$_2$Hb/THb] at each pixel. Because THb is negligible in tissue space (hemoglobin exists in blood vessels only), we used THb to segment the blood vessels and create a map of vascular HbSat.
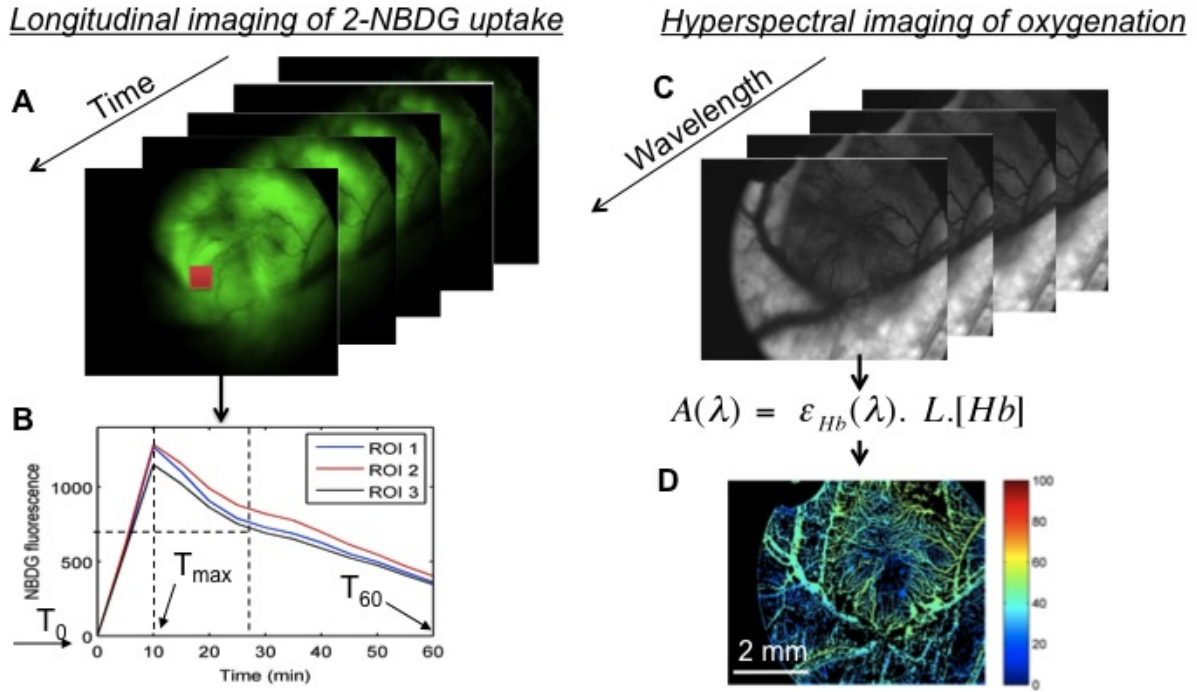

Figure 3.2: Multi-parametric quantitative visualization of imaging parameters. A) 2-NBDG fluorescence images are acquired continuously for a period of 75 minutes to construct a (x,y,l) data cube. B) At each (x,y) pixel location, a time course of 2-NBDG uptake can be obtained. C) Trans-illumination image cube of hemoglobin absorption is obtained from 520-620 nm and D) hemoglobin saturation is calculated pixel-wise by fitting a Beer-Lambert equation to the hyperspectral dataset. Total hemoglobin content [Hb] is used to threshold and create a vascular saturation map.

Optical spectroscopy of oxygen saturation and glucose uptake

A commercial fluorometer (SkinSkan, J.Y. Horiba, Edison, NJ) coupled to a fiber optic bundle was used for all the reflectance and fluorescence measurements (Fig. 3.3A). The instrument coupled the excitation to the sample and collected detected light from the sample via a bifurcated fiber optic probe bundle. Repeated reflectance and fluorescence spectra were measured from both the phantom and animal models. Reflectance and fluorescence scans from the phantoms were obtained by placing the optical probe just beneath the surface of the liquid with the phantom being stirred using magnetic stirrers the entire time to prevent polystyrene spheres from settling. The optical measurement protocol for the animal tumors was as follows: The animals were anesthetized via Isoflurane breathing (1.5% Isoflurane gas mixed with

oxygen) throughout the course of the optical measurements. Reflectance and fluorescence spectra were acquired sequentially from the tumor for 80 minutes (with a cycle time of 100s) by gently pushing the probe to make contact with the tumor and stabilizing it using a clamp during the measurements. Reflectance spectra were acquired from 450 – 650 nm and fluorescence emission spectra were acquired from 510 – 600 nm using excitation at 490 nm. An excitation wavelength of 490 nm was used rather than 470 nm as in 2-NBDG phantom studies to minimize endogenous FAD contribution. Prior to 2-NBDG injection, baseline reflectance and fluorescence spectra were measured from the tumor site. All the measurements for both phantom and animal studies were acquired in a dark room. An MC model of reflectance developed in our lab was fit to the reflectance data to extract absorption and scattering-based optical properties[47]. These optical properties were used to correct the raw fluorescence measurements for the effects of absorption and scattering to extract the corrected or intrinsic fluorescence of 2-NBDG using the MC fluorescence model. A flowchart of the model-based extraction is depicted in Fig. 3.3b [48].
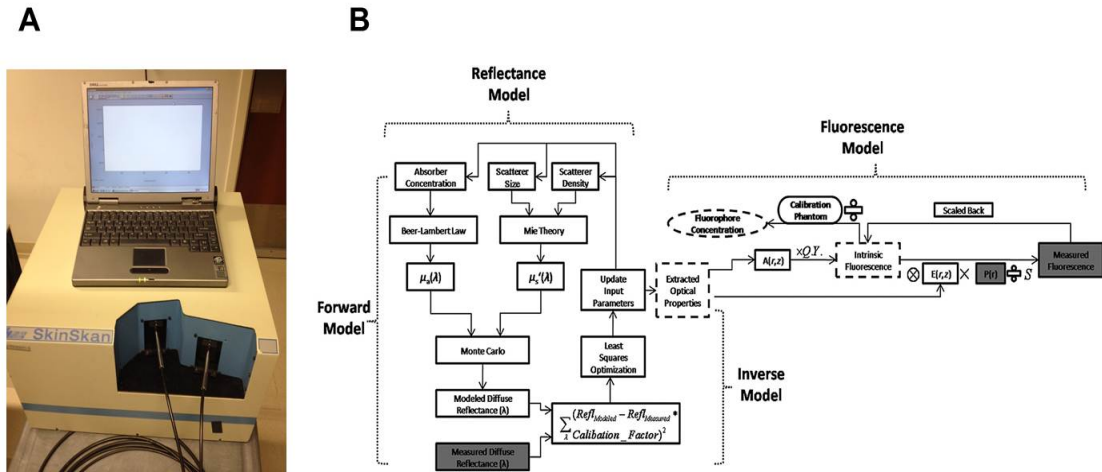

Figure 3.3: OPT-SPX instrumentation and algorithm. A. OPT-SPX instrument used to collect serial reflectance and fluorescence measurements in pre-clinical and clinical models. B. Flowchart describing the extraction of tissue optical properties and fluorophore concentrations. MC model of reflectance is initially fit to measured reflectance spectra to estimate optical properties such as scattering coefficient, Total hemoglobin and SO_2. These optical properties are used to remove scattering and absorption effects from measured fluorescence. The resulting intrinsic fluorescence is compared to a calibrated fluorescence tissue phantom to extract fluorophore concentrations.

Results:

4T1 and 4T07 cells exhibit a monotonic increase in 2-NBDG fluorescence with incubation

Figures 3.4A and 3.4B present the dynamics of 2-NBDG uptake and retention by 4T1 and 4T07 cells *in vitro*. The data show a monotonic increase in 2-NBDG fluorescence with increasing incubation times for both cell lines. This uptake pattern is strikingly similar to the study by O'Neil et al.[49] using MCF7 cells that showed a similar trend with a minor decrease in fluorescence around 10 minutes. Once inside the cells, 2-NBDG uptake is fairly constant over a time course of 60 minutes.
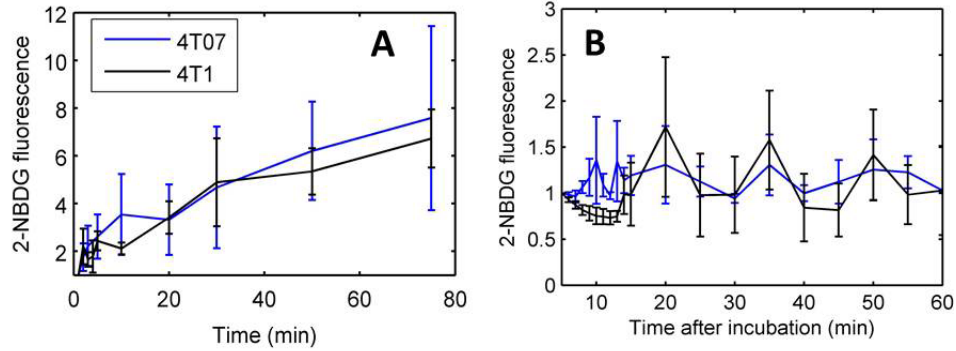
Figure 3.4: 2-NBDG uptake characteristics *in vitro*. A. 2-NBDG uptake kinetics for 4T1 and 4T07 cells. Cell plates were incubated with 2-NBDG for a period of 1-75 minutes, washed after each time point (ex. 1,2,3,4 10, 20 min) and imaged for 2-NBDG fluorescence. B. 2-NBDG retention in cells after incubation for 20 minutes. Cells were washed after incubation and imaged continuously for 60 minutes. Data are normalized to initial fluorescence measured immediately after washing.

2-NBDG fluorescence accumulates *in vivo* 50 minutes after injection

To image 2-NBDG *in vivo*, it is necessary to account for the kinetics of its vascular uptake and transport to the cells. Thus, a time point for measurement after injection was identified that would be free of the effects of wash in and wash out of 2-NBDG. Figure 3.5 shows confocal imaging of a dorsal window chamber with a 4T1 tumor. Constitutive RFP expression allows for visualization of the tumor cells at high resolution in the red fluorescence channel. At 15 minutes after injection, 2-NBDG is present in the entire field of view and is not confined to tumor cells. By 30 minutes, 2-NBDG is starting to clear from the tumor. A clump of cells in the lower left corner helps better visualize this phenomenon. The third and fourth columns present higher resolution images from this region of interest. After 40 minutes, 2-NBDG fluorescence as presented in the green channel shows good co-registration with the RFP signal. The images show that non-specific 2-NBDG fluorescence (in areas with no RFP signal) is nearly absent at 50 minutes. These data are consistent with results shown by Sheth et al.[50], who demonstrated good co-registration of tumor cells and 2-NBDG fluorescence in window chambers 50 minutes after injection. We also measured the mean 2-NBDG fluorescence from the tumor region in each window chamber as a function of time and found that 2-NBDG fluorescence reached a plateau at approximately 60 minutes (data not shown). Therefore, for all measures of 2-NBDG fluorescence, we used the measurement at 60 minutes.
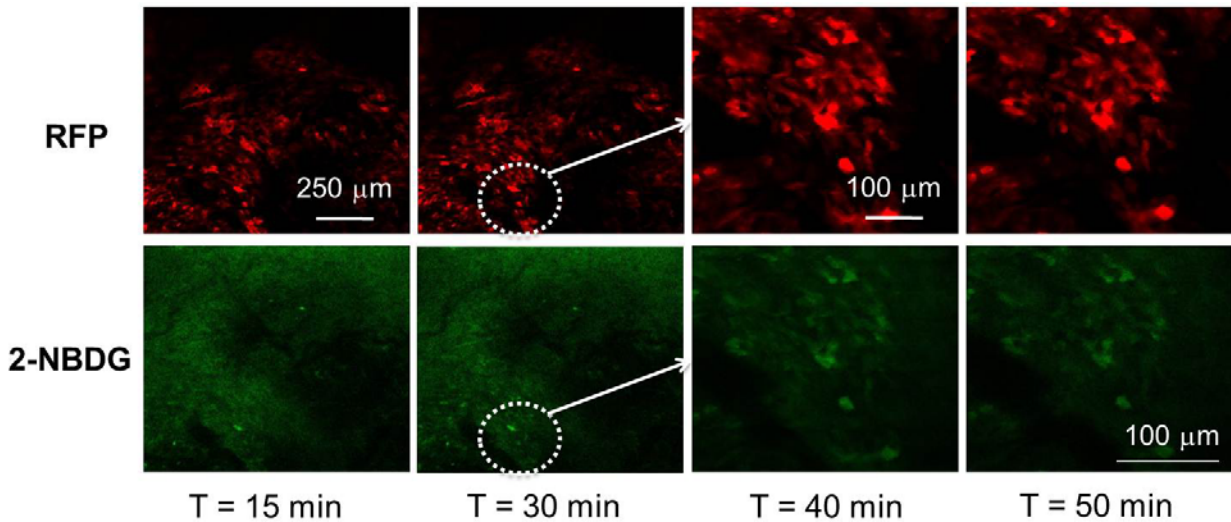
Figure 3.5: 2-NBDG localization *in vivo*. Confocal imaging of a dorsal skin flap window chamber with a 4T1 tumor. Red fluorescence is due to constititutive expression of RFP in 4T1 cells. 2-NBDG images show cellular accumulation and co-registration with RFP at 50 minutes. Note that first two columns at 15 and 30 minutes are at lower resolution (scale bar is 250 μm) and the third and fourth columns are higher resolution images (scale bar is 100 μm). These images are from the dotted ROI shown in column 2.

4T1 tumors are more hypoxic and glycolytic than 4T07 tumors

Figure 3.6 shows representative images of vascular and metabolic profiles of a normal window chamber and 4T1 and 4T07 tumors at baseline. Panel A presents hemoglobin oxygen saturation (SO_2) maps calculated from the hyperspectral trans-illumination image cube. 4T1 tumors possess a hypoxic core and a steep gradient in SO_2 towards the center of the tumor. Constitutive RFP fluorescence (not shown here) confirms that the tumor core is not necrotic. In comparison, 4T07 tumors show a well-perfused vasculature and a less evident gradient in SO_2 towards the center of the tumor. Panel B presents 2-NBDG fluorescence at 60 minutes relative to the baseline background fluorescence (measured before injection). The 4T1 tumor continues to express high 2-NBDG fluorescence after 60 minutes compared to 4T07 tumors. This demonstrates a high demand for glucose in the 4T1 tumors compared to the 4T07 tumors. It is also important to note that the normal window shows nearly negligible 2-NBDG fluorescence at 60 minutes. Normal tissue should demonstrate a 'lesser need' for 2-NBDG in the absence of any hypoxic stress or tumor burden. Panels C and D represent the rates of uptake and decay of 2-NBDG. The rate of uptake in 4T07 tumors appears to be much greater than 4T1 tumors. However, the rate of decay of 2-NBDG fluorescence is similar in both cell lines.
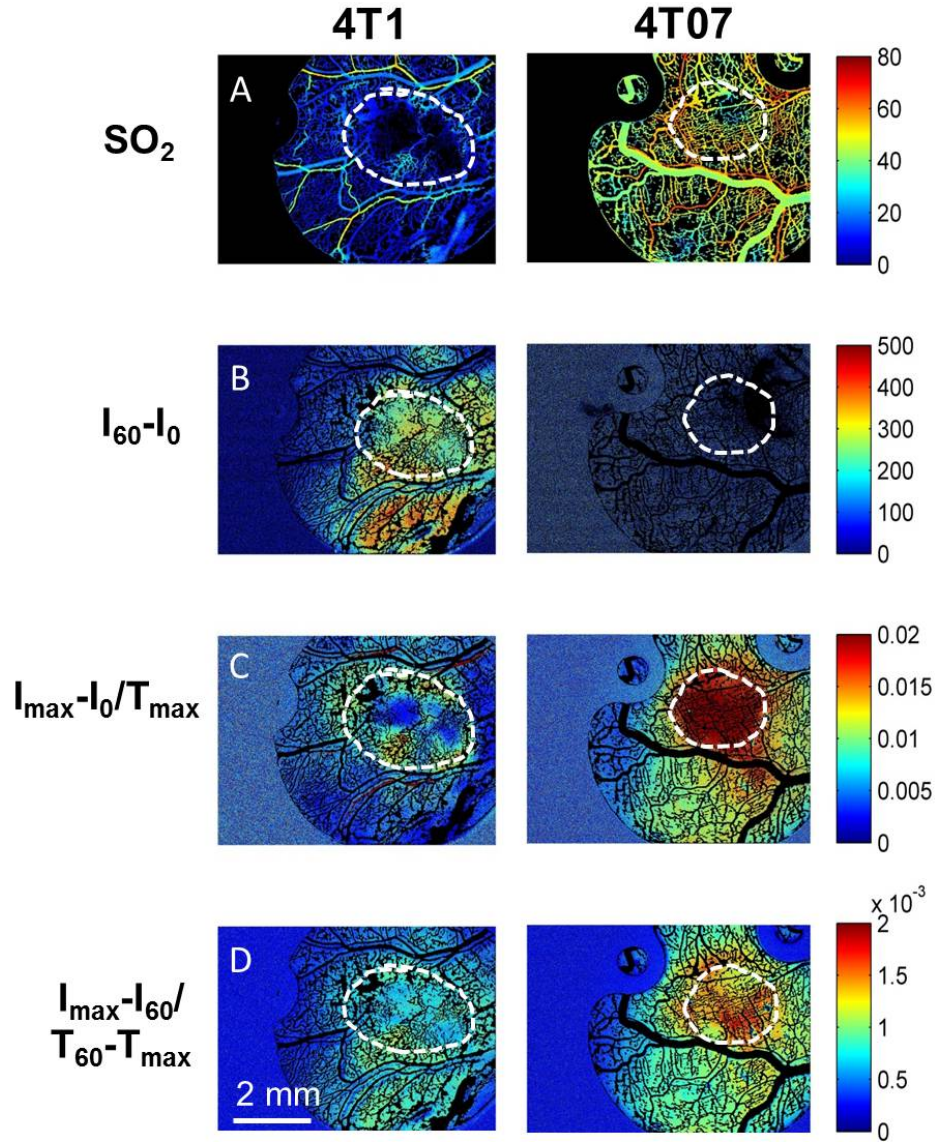
Figure 3.6: Multi-parametric imaging of 4T1 and 4T07 microenvironments at baseline. Panel A illustrates hemoglobin saturation maps from a 4T1 and a 4T07 tumor. 4T1 tumors have a well-defined hypoxic core while 4T07 tumors are well perfused. Panel B presents 2-NBDG fluorescence from the tumors at 60 minutes. Here I_0 represents non-zero background fluorescence from the tumor. The 4T1 tumor retains a high level of 2-NBDG fluorescence even at 60 minutes. C) The rate of uptake is visually higher in the 4T07 tumor and can be explained by well-perfused nature of the tumor. D) The rate of decay is calculated using the 2-NBDG fluorescence at maximum uptake and at 60 minutes and appears to be higher in 4T07 tumors. All metabolic parameters are calculated only in the tissue space. White dotted line denotes tumor.

Intermittent hypoxia causes a significant increase in 2-NBDG uptake *in vitro*

Intermittent hypoxia causes a statistically significant increase in 2-NBDG fluorescence in 4T1 and 4T07 cells (Fig. 3.7A). However, the magnitude of increase is similar in both cell lines.

Western blots of HIF-1α protein expression demonstrate a slight increase in HIF-1 in 4T07 cells (Fig. 3.7B) and no increase in HIF-1 in 4T1 cells after intermittent hypoxia.
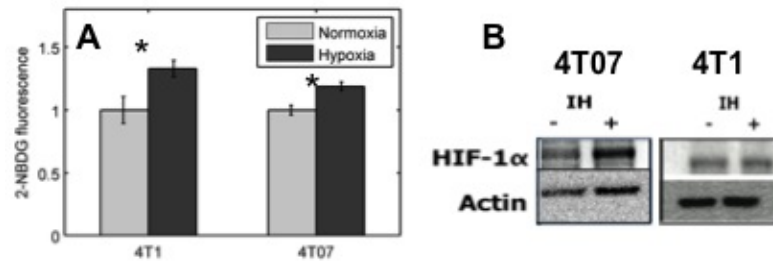

Figure 3.7: 2-NBDG uptake increases in response to intermittent hypoxia. A. Average 2-NBDG uptake in 4T1 and 4T07 cells after hypoxia is significantly higher compared to baseline (n = 3; p < 0.05). B. Western blots showing HIF-1 activity at baseline and after hypoxia for 4T1 and 4T07 cells. 4T1 cells show a negligible change in HIF-1 expression after hypoxia. 4T07 cells show a slight increase in HIF-1 activity after hypoxia. Error bars represent standard deviation of the mean. * indicates p-value < 0.05.

Intermittent hypoxia significantly increases tumor SO_2 in 4T1 tumors

Figure 3.8 shows representative images of vascular oxygen saturation (SO_2) of 4T1 and 4T07 tumors at baseline and in response to intermittent hypoxia (IH). As noted in the methods section, SO_2 measurements are made after completion of the IH regimen and not during IH itself. 4T1 tumors possess a hypoxic core and a steep gradient in SO_2 towards the center of the tumor. Constitutive RFP fluorescence (not shown here) confirms that the tumor core is not necrotic. Forced IH significantly improves the SO_2 of the 4T1 tumor (Figure 4; p<0.02). A statistical analysis of various vascular parameters revealed no significant vasodilation or change in vascular length density in 4T1 tumors post IH (data not shown). In comparison, 4T07 tumors show a well-perfused vasculature and lack of a distinct gradient in SO_2 towards the center of the tumor, and the SO_2 of the 4T07 tumor appears to be relatively unaffected by IH. There is no potential cross-talk between SO_2 and 2-NBDG fluorescence with these measurements because SO_2 measurements are made just prior to 2-NBDG injection.
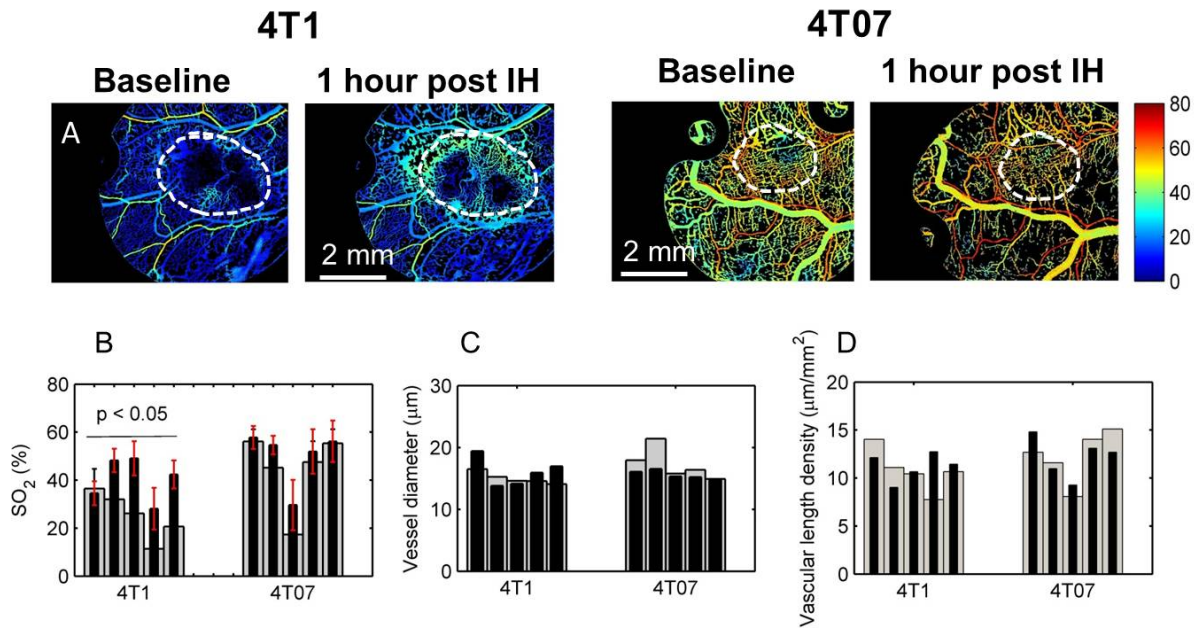
Figure 3.8: Forced intermittent hypoxia causes a significant increase in vascular saturation (SO_2) of 4T1 tumors. Panel A illustrates hemoglobin saturation maps from 4T1 and 4T07 tumors. 4T1 tumors have a well-defined hypoxic core at baseline while 4T07 tumors are well perfused. Forced intermittent hypoxia improves the vascular saturation of 4T1 tumors but has no significant effect on 4T07 tumors. B. Data reveal a significant increase ($p = 0.02$) in SO_2 in 4T1 tumors. There is no significant change in SO_2 of 4T07 tumors. IH does not cause a significant change in either C. vessel diameter or D. vascular length density in both 4T1 and 4T07 tumors post IH. Error bars represent standard deviation of the mean.

Global averages of data reveal heterogeneities in SO_2-2-NBDG relationship within tumor groups

Figure 3.9 presents the relationship between SO_2 and 2-NBDG fluorescence for each 4T1 and 4T07 tumor before and after hypoxia. Figure 3.9A presents an interesting mix of 4T1 tumors that exhibit three different metabolic effects: the Pasteur effect, Warburg effect and perfusion-mediated changes. For tumor 1 (in the order shown in figure), there is no change in vascular SO_2 after IH; however, there is a decrease in 2-NBDG relative to baseline. Tumor 2 shows a large increase in SO_2 but no change in 2-NBDG, which is indicative of the Warburg effect. Tumors 3, 4, and 5 show large increases in SO_2 after IH that are matched by a corresponding decrease in 2-NBDG. These tumors indicate that their high glycolytic activity could have been due to their hypoxic microenvironments with an increase in SO_2 due to IH reducing their need for 2-NBDG (glucose). The 4T07 tumors paint a slightly different picture. Tumor 1 saw no increase in SO_2 but an increase in 2-NBDG. A marginal increase in SO_2 for tumor 2 was sufficient to cause a large decrease in 2-NBDG. Tumors 4 and 5 saw no change in vascular SO_2 and hence no change in 2-NBDG. For all tumors, the mean saturation and mean 2-NBDG fluorescence values were calculated over a select region of interest that was identified as the tumor from constitutive RFP expression (4T1) or hemoglobin absorption images (4T07). Such a calculation results in the loss of spatial information from the tumor. In light of such large variations in the global relationship between oxygenation and glucose uptake, it is imperative to measure the relationship between the two parameters as a function of distance from blood vessel.
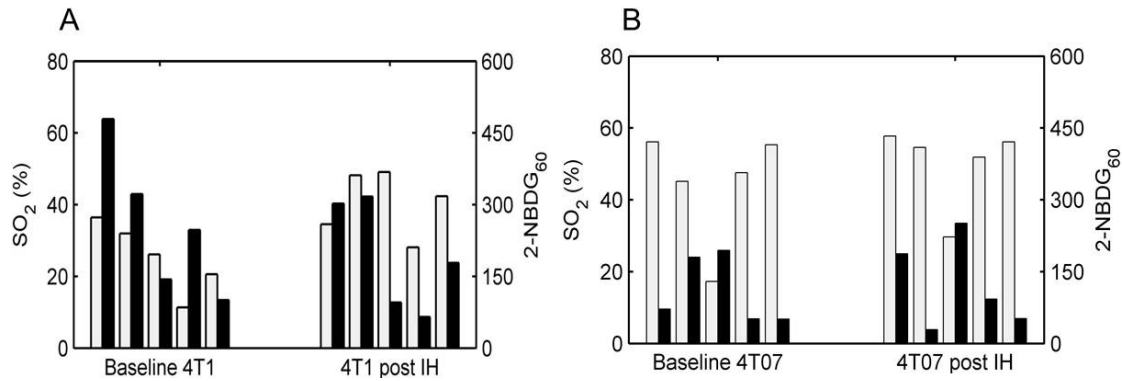
Figure 3.9: 4T1 and 4T07 tumors demonstrate both aerobic and anaerobic glycolysis. A and B present data from 4T1 and 4T07 tumors, respectively. Black bars correspond to mean 2-NBDG and grey bars represent mean SO_2 calculated over the tumor area for each animal.

4T1 tumors reveal spatial heterogeneities in 2-NBDG uptake that are SO_2 dependent.

Figure 3.10 presents cumulative distribution functions (CDF) of 2-NBDG fluorescence in different SO_2 ranges at different distances from blood vessels for 4T1 tumors. Distance ranges for both tumor groups are calculated as tertiles of pixels to avoid bias in any one range due to number of pixels. This way, each distance range shown has the same number of pixels that are distributed in different SO_2 ranges. The y-axis indicates the percentage of pixels that are below a given value. At baseline, 2-NBDG fluorescence is nearly independent of SO_2 when SO_2 is greater than 20% and this is true for all distance ranges. The Kolmogorov-Smirnov test for comparing distributions confirmed that there were no significant differences (p > 0.05) between the different saturation curves (>20%) at all distances. However, at distances very close to a blood vessel (< 15 μm), 2-NBDG fluorescence decreases when SO_2 decreases below 10% as evidenced by the left shift of the curve. Statistical analysis confirmed that 2-NBDG distribution for SO_2 less than 10% was indeed significantly lower than all other CDFs (p=0.0038) at all distances. There is no significant difference between the 2-NBDG CDFs less than 10% at different distances (p = 0.35) although the larger distances (3.10B and 3.10C) have a lower percentage of low 2-NBDG regions (red arrow). Post IH, there appears to be no significant change in 2-NBDG as a function of SO_2 at all distances. Because there is a significant increase in SO_2 of 4T1 tumors post IH, there are no vascular regions demonstrating SO_2 less than 10%.
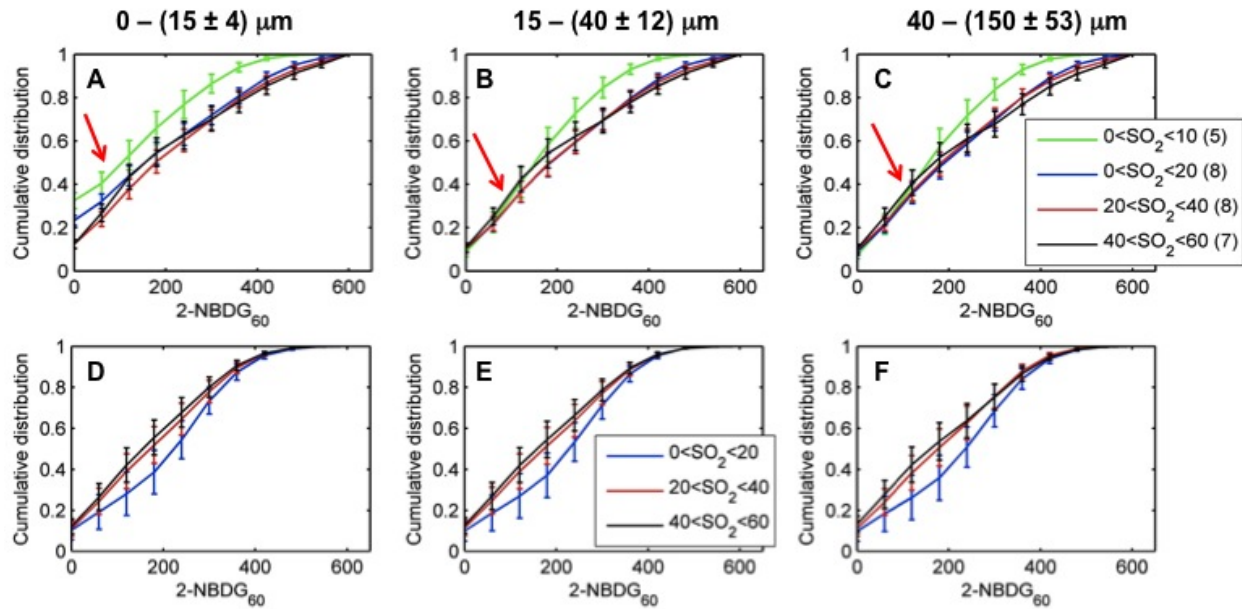
Figure 3.10: 4T1 tumors reveal spatial heterogeneities in metabolic demand that are SO_2 dependent. A-C. At baseline, 2-NBDG fluorescence is lower close to a blood vessel when SO_2 is less than 10%. D-F. 2-NBDG uptake of 4T1 tumors in response to IH as a function of SO_2 at different distances. Red arrow indicates area that is different at distances close to a blood vessel (6A) when compared to larger distances. 2-NBDG CDF at SO_2 less than 10% was significantly different from other cuves at all distances (p < 0.05). Statistical analysis to compare distributions was conducted using a Kolmogorov-Smirnov test. For each SO_2 range, the number of animals in that group is indicated in parentheses. Errors represent standard error of the mean.

Figure 3.11 illustrates the spatial metabolic profile of 4T07 tumors at baseline and post IH as a function of SO_2. There are fewer saturation ranges in the 4T07 tumors owing to its high saturation and lack of vascular heterogeneity, unlike the 4T1 tumors. Tumor regions present in the SO_2 range of 40 to 80% have very similar 2-NBDG CDF profiles (p>0.05; Kolmogorov Smirnov test). At baseline, when SO_2 is less than 60%, 2-NBDG fluorescence is nearly independent of SO_2. When SO_2 is greater than 80%, there is a corresponding decrease in 2-NBDG fluorescence as illustrated by the right shift in the 2-NBDG CDF, which can be attributed to the Pasteur effect. This data is in contrast to the 4T1 tumors which indicate a left shift or reduction in 2-NBDG fluorescence at very low SO_2, potentially indicating poor perfusion or metabolic conservation to spare glucose for other cells that are farther away. Post IH, 2-NBDG fluorescence is independent of SO_2 and presents no significant differences between the different SO_2 ranges at all distances.
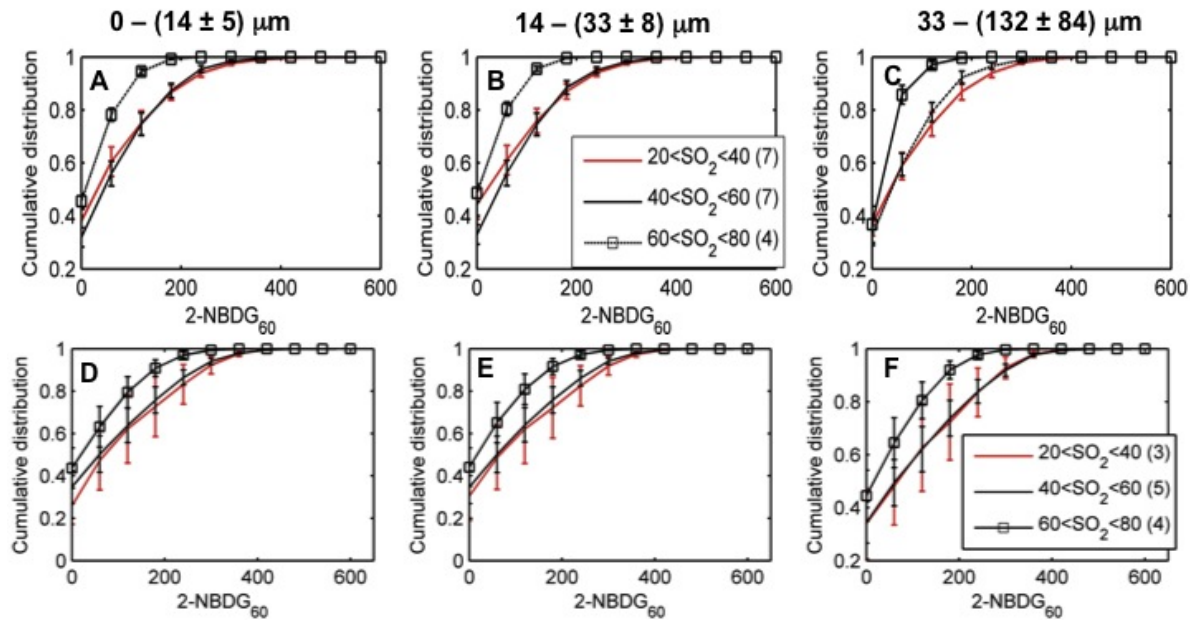
Figure 3.11: A-C. CDFs of 2-NBDG fluorescence in 4T07 tumors at baseline for different SO_2 and distance ranges. **D-F**. 2-NBDG fluorescence of 4T07 tumors in response to IH as a function of SO_2 at different distances. Statistical analysis to compare distributions was conducted using a Kolmogorov-Smirnov test. For each SO_2 range, the number of animals in that group is indicated in parentheses. Errors represent standard error of the mean.

<u>Optical spectroscopy is sensitive to changes in 2-NBDG concentration [51]</u>

Fig. 3.12(a) shows the measured fluorescence intensity change over time and Fig. 3.12(b) shows the same data for extracted intrinsic fluorescence for all mice. The 2-NBDG peak fluorescence wavelength (545 nm) was used at each time point for all plots. For a given 2-NBDG dose, the measured and extracted fluorescence first increase to a maximum and then decreases due to 2-NBDG uptake by the cells. More importantly, there is a progressively increasing trend with increasing 2-NBDG dose in the extracted intrinsic fluorescence. However, this is not observed in the raw fluorescence. Fig. 3.12(c) shows the scatter plot of measured fluorescence intensity as a function of injected 2-NBDG dose at three time points (t20, t40 and t60) and Fig. 3.12(d) shows the same data for extracted intrinsic fluorescence for all mice. The error bar indicates the standard deviation in each 2-NBDG concentration group. The r value at the top of each figure is the Pearson's linear correlation coefficient of the three doses at each time point and the coordinate origin (0,0). We can ascertain from these values that the linearity of intrinsic fluorescence is clearly more significant than that of the measured fluorescence. Moreover, variations within the same dose group are smaller for intrinsic fluorescence than measured fluorescence.
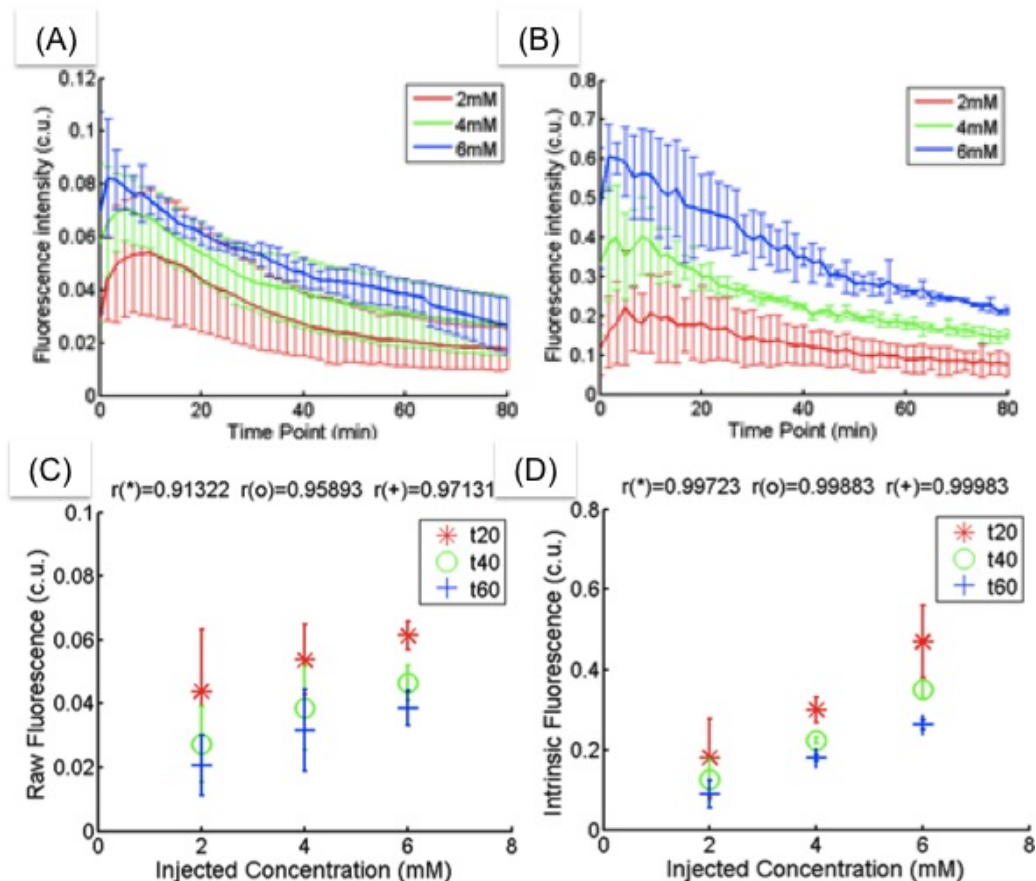
Figure 3.12: Optical spectroscopy is sensitive to *in vivo* changes in 2-NBDG uptake in tumors. A. Average measured fluorescence measured from tumors for different doses of injected 2-NBDG. There are no significant differences in the average spectra for different dosing groups. B. Average corrected fluorescence for each injected dose showing significant separation between the injected doses at later time points (t > 40 minutes). C. Raw fluorescence at specific time points for the different doses. Correlation between fluorescence and injected dose increases with time. D. Corrected fluorescence at specific time points for the different doses. Correlation between corrected fluorescence and injected dose increases with time and is higher than correlations for raw fluorescence.

Plans for year 4:

Our research strategy going forward involves the study of basic biological phenomena in *in vitro* and pre-clinical animal models and translating relevant endpoints to clinically viable optical spectroscopy instruments. We will establish the metabolic profile of cell lines *in vitro* (in the absence of a microenvironment), study the spatiotemporal relationships between oxygenation and glucose uptake in pre-clinical dorsal skin flap models and determine clinical feasibility in pre-clinical tumor xenograft models. We plan to study the response of human breast cancer cell lines to hypoxic stress that was shown here to distinctly perturb only the metastatic phenotype. These studies will be conducted *in vitro* and in skin flap window chamber models. In addition, we will study the changes to tumor microenvironment in response to stresses that are known to change tumor phenotype.

In year 4, we plan to extend our optical spectroscopy studies to identify optimal time points for

imaging. Specifically, we will optimize the fasting duration for mice to ensure 2-NBDG reports on glucose uptake *in vivo*, identify the ideal dose of 2-NBDG to be injected in tumors and determine the optimal time point after injection that reports on 2-NBDG uptake by cells. We plan to conduct pre-clinical studies on mice to determine whether combined knowledge of both oxygen saturation and glucose uptake can improve the predictive value of response to therapy compared to either one parameter alone.

3. KEY RESEARCH ACCOMPLISHMENTS:

AIM 1

- Advanced optical imaging for breast margin assessment through analysis of potential sources of error (excisional time, cautery, and patent blue dye) on underlying sources of optical contrast
- Determined that the choice of wavelength-dependent scattering model had little effect on extracted optical properties, suggesting that current model is sufficient for obtaining accurate optical parameters.
- Acquired images using the 49-channel system in 54 patients undergoing partial mastectomy, mastectomy or reduction mammoplasty. Of these samples, 29 have been imaged by the high resolution microendoscope
- Developed analysis software to invert diffuse reflectance measurements and process extracted parameter maps from the 49-channel system.

AIM 2

Duke
- Completed a large *ex vivo* biopsy study which demonstrates the potential of using HRME imaging to determine histology of samples during a core needle biopsy procedure.
- Applied sparse decomposition algorithm to images of biopsy specimens and showed potential of using it to distinguish between malignant and benign tissue.

Rice
- Acquired images from resected tumor and needle biopsy specimens. To date, we imaged a total of 126 specimens from 64 patients. Images were obtained using both a commercial laser scanning confocal device and the HRME described in the original proposal.
- Assembled images into a library of normal, non-neoplastic features and neoplastic lesions to facilitate comparison between high resolution optical images and the corresponding histological sections.
- The images in the library have been organized into a training set and a validation set to test the accuracy of confocal fluorescence microscopy compared to the reference standard, histologic assessment and have begun quantitative evaluation of morphologic features, including adipocyte size and density.

AIM 3

- Demonstrated the feasibility of measuring spatiotemporal relationships between oxygen saturation and glucose uptake *in vivo* at high resolution.
- Identified significant differences in tumor microvasculature and metabolic demand of sibling cell lines that differ in metastatic potential and their response to hypoxic stress
- Demonstrated the ability of optical spectroscopy to measure *in vivo* changes in 2-NBDG concentration as a function of injected dose.

4. REPORTABLE OUTCOMES:

Journal publications – (published, in review and in progress)

1. J. Quincy Brown and Torre M. Bydlon, Stephanie A. Kennedy, Matthew L. Caldwell, Jennifer E. Gallagher, Marlee Junker, Lee G. Wilke, William T. Barry, Joseph Geradts, <u>Nimmi Ramanujam</u>. "Leveraging Tissue Composition and Micromorphology for Breast Tumor Margin Assessment via Quantitative Diffuse Optical Spectral Imaging." (*in progress*)
2. Bydlon TM, Barry WT, Kennedy S, Brown JQ, Gallagher J, Wilke L, Geradts J, <u>Ramanujam N</u>.. "Advancing optical imaging for breast margin assessment: an analysis of excisional time, cautery, and patent blue dye on underlying sources of contrast." PLoS One (*under review*)
3. Kennedy S, Geradts J, Caldwell M, Bydlon M, Mulvey C, Mueller J, Barry W, <u>Ramanujam N</u>, "Using Breast Tissue Histology to Understand Optical Signatures and Improve Optical Margin Assessment." Breast Cancer Research. (*submitted*).

Conference abstracts and proceedings

1. Kennedy S, Mueller J, Bydlon T, Brown JQ, Ramanujam N, "Using wide-field quantitative diffuse reflectance spectroscopy in combination with high-resolution imaging for margin assessment," *Proc. SPIE* 7890, Advanced Biomedical and Clinical Diagnostic Systems IX, 78900C (February 23, 2011); doi:10.1117/12.875735

AIM 2:

Journal publications – (published, in review and in progress)

1. Mueller J, Harmany Z, Mito K, Kennedy S, Kim Y, Dodd L, Geradts J, Kirsch D, Willett R, Brown Q, Ramanujam N. *Quantitative segmentation of fluorescence microscopy images of heterogeneous tissue: Application to the detection of residual disease in tumor margins.* PLoS ONE, 2012. Submitted.

Conference abstracts and proceedings

1. Harmany Z, Mueller J, Brown Q, Ramanujam N, Willett R. *Tissue quantification in photon-limited microendoscopy.* Applications of Sparse Representations in Bioimaging SPIE Proceedings Vol. 8138, 81380F (2011);
2. Mueller J, Harmany Z, Mito K, Kennedy S, Kim Y, Dodd L, Geradts J, Kirsch D, Willett R, Brown Q, Ramanujam N. *Quantitative segmentation of fluorescence microscopy images*

of heterogeneous tissue: Application to the detection of residual disease in tumor margins. SPIE Photonics West, *San Francisco, CA*, February 2013.

3. J. Dobbs, H. Ding, A, Benveniste, H. Kuerer, S. Krishnamurthy, W. Yang, R. Richards-Kortum. "Confocal Fluorescence Microscopy for Evaluation of Breast Cancer in Human Breast Tissue." Biomedical Optics – Optics Society of America. Miami, FL. May 1, 2012.
4. J. Dobbs, H. Ding, A, Benveniste, H Kuerer, S. Krishnamurthy, W. Yang, R. Richards-Kortum. "Confocal Fluorescence Microscopy for Real-Time, High-Resolution Assessment of Breast Cancer Morphology." BioMedOpTex Symposium. Texas A&M University, College Station, TX. May 24, 2012.

AIM 3:

Journal publications – (published, in review and in progress)

1. Liu C, Rajaram N, Vishwanath K, Jiang T, Palmer G, <u>Ramanujam N</u>. Experimental validation of an inverse fluorescence Monte Carlo model to extract concentrations of metabolically relevant fluorophores from turbid phantoms and a murine tumor model. *Journal of Biomedical Optics* 17(7): 077012, 2012
2. Rajaram N, Frees AE, Zhong J, Fontanella AN, Millon SR, Hansen K, Barry WT, Dewhirst MW, <u>Ramanujam N</u>. Molecular imaging of spatiotemporal characteristics of glucose demand in murine tumors (manuscript in preparation)

Conference abstracts and proceedings

1. Rajaram N, Frees AE, Zhong J, Dewhirst MW and Ramanujam N. Molecular imaging of spatiotemporal glucose demand in tumors in vivo. Gordon Research Conference on Lasers in Medicine and Biology. Holderness, NH, Jul 22-27, 2012.
2. Frees AE, Rajaram N, Dewhirst MW and Ramanujam N. Effect of hypoxic duration on breast cancer metabolism and redox status. Keystone Symposia on Molecular and Cellular Biology: Tumor Metabolism, Banff, Alberta, Feb 12-17, 2012.
3. Rajaram N, Frees AE, Palmer GM, Dewhirst MW and Ramanujam N. Optical longitudinal imaging of tumor metabolic and vascular response to hypoxia. Keystone Symposia on Molecular and Cellular Biology: Tumor Metabolism, Banff, Alberta, Feb 12-17, 2012.

5. CONCLUSIONS:

Aim 1

From the current study we determined that HbSat cannot be fit with a linear model due to excessive changes in oxygenated and deoxygenated hemoglobin post-excision. This is likely due to oxygen being consumed by the metabolically active tissue immediately after excision. Although HbSat may be a useful *in vivo* parameter for determining tumor hypoxia, or for examining the local microenvironment, or even for margin assessment of the resected cavity, it is not reliable in *ex vivo* margin assessment of breast tissue specimens. The results from both the simulated and phantom data for [patent blue dye] indicate that [patent blue dye] up to 80µM does not impact the extractions of [THb], [β-carotene], or $<\mu_s'>$ from the diffuse reflectance spectra; again, the highest concentration of patent blue dye seen in the previous lumpectomy study was 72.7µM. Although the errors were higher in the phantom data (as would be

expected), there was no trend in the percent error with increasing [patent blue dye]. In terms of tissue cauterization, we found that initial measurements of [THb] were significantly higher in the benign sites of the cauterized lumpectomies compared to the mastectomies. This initial difference could be due either to varying excisional times for mastectomy and lumpectomy procedures or due to cauterization. Since we observed no significant correlation between the initial value and time from excision, we assume that this difference in [THb] is due to cauterization of the vasculature to prevent blood from draining out of the vessels as rapidly as it would in mastectomy specimens. For all tissue parameters, the rate of change was not significantly different between the benign and malignant sites. This is an important finding for margin assessment which indicates that optical contrast between benign and malignant regions of a margin will be preserved, regardless of the time when the margin is imaged over a 30 minute window. We also showed that there was no correlation between the time from excision and the initial value (or first measurement) of the optical data. This suggests minimal change in the data within the time window that we examined (17±4 minutes post-excision and measured for 10-32 minutes). Additionally since there was no significant difference between the lumpectomies and mastectomies for [β-carotene] and [β-carotene]/$<\mu_s'>$, we can extrapolate these findings to benign and malignant tissue in cauterized lumpectomies.

Collagen and glands were both contributors to scattering; in malignant sites however, the glandular component was more strongly correlated. Scattering from collagen also exhibited a relationship to age where it was increased in sites from young patients with a higher percentage of collagen but decreased in older women. This information will help develop improved scattering models and additional technologies to separate fibroglandular sites from malignant sites and ultimately improve margin assessment.

Further, we have also determined that the choice of scattering model has little effect on the optical properties extracted from diffuse reflectance spectra, so we will continue to utilize a Mie model for the remainder of this study.

Aim 2

Duke
The *ex vivo* biopsy study demonstrates that high resolution fluorescence imaging of acriflavine stained tissue combined with an algorithm that leverages sparse decomposition analysis and circle transform (SD+CT) provides a rapid, non-destructive and automated strategy for quantitative pathology of thick tissues with non-uniform background heterogeneity. We will identify additional endpoints/parameters that have diagnostic potential (such as the size of nuclei), and build predictive models that can quantitatively diagnose high resolution images in Year 4.

Rice
Using both a commercial laser scanning confocal device and the HRME, we have found correlations between morphologic biomarkers assessed from high resolution optical images (epithelial cell density and N/C ratio; collagen density, fiber size, fiber linearity; adipocyte size and density) and histologic diagnosis and biomarkers of cancer risk and progression. We have also defined metrics of breast density which can be calculated from high resolution optical

images of breast tissue and correlate with histologic diagnosis, biomarkers of cancer risk and progression.

Aim 3

Although a number of studies have illustrated the significance of the Warburg effect and its relationship to tumor aggressiveness, a majority was conducted in cell culture in the absence of a true microenvironment. Also, there are a few studies on the other end of the spectrum, examining the relationship between glucose uptake and oxygenation in patients. However, current whole body imaging techniques such as FDG-PET imaging for glucose uptake and contrast-enhanced MRI for tissue hypoxia are not well suited for repeated measures on the same tumor at frequent intervals and lack sufficient spatial resolution to evaluate spatiotemporal relationships in the tumor microenvironment. High-resolution imaging of glucose uptake and vascular oxygenation status, as described here can provide unprecedented spatial information and help us understand the relationship between both parameters. Intravital microscopy can provide quantitative measures of *in vivo* tumor biomarkers, either endogenous or exogenous. It is noninvasive, permitting short-term repeated measurements on the same animal can continuously monitor changes in tumor microvasculature and more importantly study, at a high resolution, the cells adjacent to these blood vessels. Our results indicate differences in tumor metabolic response to stress, depending on their phenotype. Because the type of stress has been linked to long-term tumor behavior, understanding the metabolic response provides us with a vital endpoint that could help clinically predict a tumor's propensity for radio- or chemo-resistance, metastasis or recurrence. Toward this end, we have demonstrated the ability of optical spectroscopy and our models to extract *in vivo* oxygenation and 2-NBDG uptake as a function of injected dose.

6. REFERENCES:

1. Jacobs, L., *Positive margins: the challenge continues for breast surgeons.* Ann Surgical Oncology, 2008. **15**(5): p. 1271-2.
2. Lee, M.C., et al., *Determinants of breast conservation rates: reasons for mastectomy at a comprehensive cancer center.* Breast J, 2009. **15**(1): p. 34-40.
3. Society, A.C. *Cancer Facts and Figures 2009.* 2009.
4. Sanchez, C., et al., *Factors associated with re-excision in patients with early-stage breast cancer treated with breast conservation therapy.* Am Surg, 2010. **76**(3): p. 331-4.
5. Mann, R.M., et al., *The impact of preoperative breast MRI on the re-excision rate in invasive lobular carcinoma of the breast.* Breast Cancer Res Treat, 2010. **119**(2): p. 415-22.
6. Balch, G.C., et al., *Accuracy of intraoperative gross examination of surgical margin status in women undergoing partial mastectomy for breast malignancy.* Am Surg, 2005. **71**(1): p. 22-7; discussion 27-8.
7. Mendez, J.E., et al., *Influence of breast cancer margin assessment method on the rates of positive margins and residual carcinoma.* Am J Surg, 2006. **192**(4): p. 538-40.

8. Huston, T.L., et al., *The influence of additional surgical margins on the total specimen volume excised and the reoperative rate after breast-conserving surgery.* Am J Surg, 2006. **192**(4): p. 509-12.

9. Kobbermann, A., et al., *Impact of Routine Cavity Shave Margins on Breast Cancer Re-excision Rates.* Ann Surg Oncol, 2010.

10. McCahill, L.E., et al., *Variability in reexcision following breast conservation surgery.* JAMA, 2012. **307**(5): p. 467-75.

11. Bydlon, T.M., et al., *Performance metrics of an optical spectral imaging system for intra-operative assessment of breast tumor margins.* Opt Express, 2010. **18**(8): p. 8058-76.

12. Wilke, L.G., et al., *Rapid noninvasive optical imaging of tissue composition in breast tumor margins.* Am J Surg, 2009. **198**(4): p. 566-74.

13. Brown, J., et al., *Optical assessment of tumor resection margins in the breast.* IEEE Journal on Selected Topics in Quantum Electronics, 2010( ): p. accepted.

14. Kennedy, S.A., et al., *Optical breast cancer margin assessment: an observational study of the effects of tissue heterogeneity on optical contrast.* breast Cancer Research, 2010. **12**(6).

15. Palmer, G.M. and N. Ramanujam, *A Monte Carlo-based inverse model for calculating tissue optical properties. Part I: Theory and validation on synthetic phantoms.* Appl. Opt., 2006. **45**(5): p. 1062-71.

16. Palmer, G.M., et al., *A Monte Carlo-based inverse model for calculating tissue optical properties. Part II: Application to breast cancer diagnosis.* Appl. Opt., 2006. **45**(5): p. 1072-8.

17. Brown, J.Q., et al., *Optical Assesssment of Tumor Resection Margins in the Breast.* Selected Topics in Quantum Electronics, IEEE Journal of, 2010. **16**(3): p. 530-544.

18. Bydlon, T.M., et al., *Performance metrics of an optical spectral imaging system for intra-operative assessment of breast tumor margins.* Opt. Express, 2010. **18**(8): p. 8058-8076.

19. Kennedy, S., et al., *Optical breast cancer margin assessment: an observational study of the effects of tissue heterogeneity on optical contrast.* Breast Cancer Research, 2010. **12**(6): p. R91.

20. Kennedy, S., et al., *Optical breast cancer margin assessment: an observational study of the effects of tissue heterogeneity on optical contrast.* Breast Cancer Res, 2010. **12**(6): p. R91.

21. Graaff, R., et al., *Reduced light-scattering properties for mixtures of spherical particles: a simple approximation derived from Mie calculations.* Appl Opt, 1992. **31**(10): p. 1370-6.

22. Brown, J.Q., *Optical Assesssment of Tumor Resection Margins in the Breast.* IEEE Journal of selected topics in Quantum Electronics, 2010. **16**(3): p. 530-544.

23. Bigio, I.J., et al., *Diagnosis of breast cancer using elastic-scattering spectroscopy: preliminary clinical results.* J Biomed Opt, 2000. **5**(2): p. 221-8.

24. Haka, A.S., et al., *Diagnosing breast cancer using Raman spectroscopy: prospective analysis.* J Biomed Opt, 2009. **14**(5): p. 054023.

25. Clark, A.L., et al., *Confocal microscopy for real-time detection of oral cavity neoplasia.* Clin Cancer Res, 2003. **9**(13): p. 4714-21.

26. Drezek, R.A., et al., *Optical imaging of the cervix.* Cancer, 2003. **98**(9 Suppl): p. 2015-27.

27. Nguyen, F.T., et al., *Intraoperative evaluation of breast tumor margins with optical coherence tomography.* Cancer Res, 2009. **69**(22): p. 8790-6.

28. Clark, A.L., et al., *Detection and diagnosis of oral neoplasia with an optical coherence microscope.* J Biomed Opt, 2004. **9**(6): p. 1271-80.

29. Karen, J.K., et al., *Detection of basal cell carcinomas in Mohs excisions with fluorescence confocal mosaicing microscopy.* Br J Dermatol, 2009. **160**(6): p. 1242-50.

30. Gareau, D.S., *Feasibility of digitally stained multimodal confocal mosaics to simulate histopathology.* J Biomed Opt, 2009. **14**(3): p. 034050.

31. Tanbakuchi, A.A., et al., *Clinical confocal microlaparoscope for real-time in vivo optical biopsies.* J Biomed Opt, 2009. **14**(4): p. 044030.

32. Muldoon, T.J., et al., *Subcellular-resolution molecular imaging within living tissue by fiber microendoscopy.* Opt Express, 2007. **15**(25): p. 16413-23.

33. Muldoon, T.J., et al., *High-resolution imaging in Barrett's esophagus: a novel, low-cost endoscopic microscope.* Gastrointest Endosc, 2008. **68**(4): p. 737-44.

34. Nyirenda, N., D.L. Farkas, and V.K. Ramanujan, *Preclinical evaluation of nuclear morphometry and tissue topology for breast carcinoma detection and margin assessment.* Breast Cancer Res Treat, 2010.

35. Starck, J.L., M. Elad, and D.L. Donoho, *Image decomposition via the combination of sparse representations and a variational approach.* IEEE Trans Image Process, 2005. **14**(10): p. 1570-82.

36. Candès, E.J. and D.L. Donoho, *New tight frames of curvelets and optimal representations of objects with piecewise C2 singularities.* Communications on Pure and Applied Mathematics, 2004. **57**(2): p. 219-266.

37. Figueiredo, M.A.T., R.D. Nowak, and S.J. Wright, *Gradient Projection for Sparse Reconstruction: Application to Compressed Sensing and Other Inverse Problems.* Selected Topics in Signal Processing, IEEE Journal of, 2007. **1**(4): p. 586-597.

38. Cohen, C., *Image cytometric analysis in pathology.* Hum Pathol, 1996. **27**(5): p. 482-93.

39. Millot, C. and J. Dufer, *Clinical applications of image cytometry to human tumour analysis.* Histol Histopathol, 2000. **15**(4): p. 1185-200.

40. Gerlinger, M., et al., *Intratumor heterogeneity and branched evolution revealed by multiregion sequencing.* New England Journal of Medicine, 2012. **366**(10): p. 883-892.

41. Hanahan, D. and R.A. Weinberg, *Hallmarks of cancer: the next generation.* Cell, 2011. **144**(5): p. 646-674.

42. Semenza, G.L., *HIF-1: upstream and downstream of cancer metabolism.* Current opinion in genetics & development, 2010. **20**(1): p. 51-56.

43. Warburg, O., *On the origin of cancer cells.* Science, 1956. **123**(3191): p. 309-314.

44. Robey, I.F., et al., *Hypoxia-inducible factor-1 and the glycolytic phenotype in tumors.* Neoplasia (New York, NY), 2005. **7**(4): p. 324.

45. Robey, I.F., et al., *Regulation of the Warburg effect in early-passage breast cancer cells.* Neoplasia (New York, NY), 2008. **10**(8): p. 745.

46. Sorg, B.S., et al., *Hyperspectral imaging of hemoglobin saturation in tumor microvasculature and tumor hypoxia development.* J Biomed Opt, 2005. **10**(4): p. 44004.

47. Palmer, G.M. and N. Ramanujam, *Monte Carlo-based inverse model for calculating tissue optical properties. Part I: Theory and validation on synthetic phantoms.* Applied optics, 2006. **45**(5): p. 1062-1071.

48. Palmer, G.M. and N. Ramanujam, *Monte-Carlo-based model for the extraction of intrinsic fluorescence from turbid media.* Journal of biomedical optics, 2008. **13**(2): p. 024017-024017-9.

49. O'Neil, R.G., L. Wu, and N. Mullani, *Uptake of a fluorescent deoxyglucose analog (2-NBDG) in tumor cells.* Molecular Imaging and Biology, 2005. **7**(6): p. 388-392.

50. Sheth, R., L. Josephson, and U. Mahmood, *Evaluation and clinically relevant applications of a fluorescent imaging analog to fluorodeoxyglucose positron emission tomography.* Journal of Biomedical Optics, 2009. **14**: p. 064014.

51. Liu, C., et al., *Experimental validation of an inverse fluorescence Monte Carlo model to extract concentrations of metabolically relevant fluorophores from turbid phantoms and a murine tumor model.* Journal of Biomedical Optics, 2012. **17**(7): p. 77012.